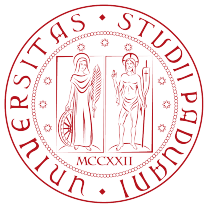

UNIVERSITÀ DEGLI STUDI DI PADOVA

Dipartimento di Fisica e Astronomia "Galileo Galilei"

Master Degree in Physics

Final Dissertation

Study of the $^{12}C(p,\gamma)^{13}N$ reaction cross section at high energies at the Felsenkeller underground facility

Thesis supervisor

Prof. Dr. Antonio Caciolli

Thesis co-supervisor

Dr. Denise Piatti

Candidate

Harshithbabu

Academic Year 2021/2022

Abstract

The $^{12}C(p,\gamma)^{13}N$ reaction has a crucial role in the determination of $^{12}C/^{13}C$ isotopic ratio in RGB and AGB H-shell. This ratio is a sensitive indicator of stellar nucleosysnthesis and a useful tool to trace the galactic evolution. However, existing models cannot reproduce the observed $^{12}C/^{13}C$ isotopic ratio due to the poorly cross section constrained extrapolations at energies of interest. In the present work the measurement of $^{12}C(p,\gamma)^{13}N$ reaction cross section, performed at the Felsenkeller underground facility in Dresden (Germany) in the energy range 350-700 keV, is presented. Prompt γ-rays associated with the formation of ^{13}N nuclide were analysed to determine the reaction cross section and the S-factor results are compared with some of the previous.

Contents

List of Figures

Chapter 1
Introduction

The source of energy emitted by stars and its evolution have puzzled scientists for many years. In 1920, F.W. Aston discovered that thermonuclear reactions could be the source of energy for stars when he observed the mass deficit between a helium atom and four hydrogen atoms. Sir A.S. Eddington proposed that the energy produced by stars comes from the fusion of hydrogen nuclei into helium.. Few years later, the feasibility of hydrogen fusion was supported by the discovery of quantum tunneling effect by G. Gamow and it was confirmed by spectroscopic observations. Nuclear reactions taking place in stellar interiors are responsible of their radiated energy, synthesis of elements and their evolution.The Nuclear Astrophysics was born.

Today, it is known that H-burning takes place in stars via two processes: The pp chain and the CNO cycle. The present work focuses indeed on the study of one of the CNO channels, the $^{12}C(p,\gamma)^{13}N$ reaction which plays a crucial role in the determination of $^{12}C/^{13}C$ isotopic ratio in the H-shell of Red Giant Branch (RGB) and Asymptotic Giant Branch (AGB). The observed $^{12}C/^{13}C$ ratio in IR stellar spectra and presolar grains is a valuable tool for tracing RGB and AGB nucleosynthesis. Moreover, during the mixing events taking place in these stars, several different isotope ratios inside the stellar atmosphere are drastically altered as the convective motion of the star mixes the CNO products with the external stellar layers. The $^{12}C/^{13}C$ isotopic ratio is indeed a perfect tool to get insights of the mixing processes main parameters. Finally RGB and AGB stars, as mass loss locations, plays the key role of interstellar medium polluters and the $^{12}C/^{13}C$ is thus a perfect tracer of Galactic Chemical Evolution.

Recent observations of the $^{12}C/^{13}C$ isotopic ratio in the atmospheres of the globular cluster giants [7] are not in agreement with the model predictions. In addition, in carbonaceous chondrite meteorites, which are believed to be derived from carbon star atmosphere, the observed $^{12}C/^{13}C$ ratios is still puzzling [8]. In order to better constraint the models, it is crucial to reduce the uncertainties affecting the $^{12}C(p,\gamma)^{13}N$ reaction rate.

Several investigations have been conducted on the $^{12}C(p,\gamma)^{13}N$ reaction over a wide energy range, with the aim of measuring the reaction cross section in the Gamow peak of RGB stars. However, due to the extremely low cross section in this energy range, it is not possible to directly measure the reaction, and the measured S-factor is usually extrapolated at low energies. Previous experiments conducted by Bailey, Hall et al., Lamb et al., Vogl, and Rolfs et al. have measured the cross section at different energy ranges, but their data have large uncertainties and little overlap in energy range. A recent measurement by Burtebaev et al. still does not solve the discrepancy observed in the lower energy resonance E_r of the reaction.

The present work deals with an experiment conducted at Felsenkeller underground facility

in Dresden (Germany) in the first half of 2022. The well collimated proton beam from 5MV Pelletron accelerator of Felsenkeller was directed on thin evaporated carbon targets (99% ^{12}C and 1% ^{13}C). An HPGe detector was used to detect the prompt γ-rays coming from the $^{12}\mathrm{C}(p,\gamma)^{13}\mathrm{N}$ reaction. Four additional HPGe detectors were added to the setup in order to cross check the angular distribution. This thesis reports the preliminary results for the $^{12}\mathrm{C}(p,\gamma)^{13}\mathrm{N}$ reaction cross section in a wide energy range,E_p = 350-700keV. The current data overlap with recent measurements from the LUNA experiment, providing a new and precise dataset for more reliable extrapolations.

The thesis is structured as follows: In chapter 2, a brief introduction to stellar nucleosynthesis processes and the formalism to treat them can be found. The reaction and the current state of art are described in chapter 3. In chapter 4, the experimental setup used for the experiment is illustrated. In chapter 5, the data analysis, methodology and results are presented. Conclusive remarks and outlooks are in chapter 5.

Chapter 2
Stellar Nucleosynthesis

Nuclear reactions are both the main stellar energy source and the leading process for chemical evolution of stars. The study of these thermonuclear reactions in the stellar medium is necessary to reconstruct their evolution and hence by extension the history of universe. Nearly all of the elements found on Earth and also in our solar system and galaxy were indeed created inside the hot interiors of the stars.

In the first section of this chapter, we will discuss some basic concepts of stellar nucleosynthesis including a brief description of the stellar evolution. The last section of this chapter is devoted to present analytical tools useful to treat the thermonuclear reactions of interest for the present work.

2.1 Nucleosynthesis

The observed abundances of the solar system show indeed that the most abundant elements are H ($\approx$ 70%) and He ($\approx$ 30%) which were produced during the Big Bang nucleosynthesis along with traces of Li, see Fig 2.1. The question that arises here is what accounts for the different abundances of the elements, Z 3 and the various processes that led to their creation. The main purpose of nuclear astrophysics is to answer this question.

For years scientists thought that the nucleosynthesis primarily occurred during the Big Bang [9]. However this theory was not able to describe the observations successfully. A fresh perspective emerged as a result of the inability to identify a single process that could account for the observed abundance of the nuclides. A variety of distinct reactions that took place in different environments and at different times in the history of the Universe gave origin to the elements in the presently observed abundances. This theory was proposed for the first time in the work of M. Burbidge, G. Burbidge, W.A. Fowler and F. Hoyle [10].

The creation of elements in the universe occurred through various processes. Cosmological Nucleosynthesis produced H, He, and some Li nuclides shortly after the Big Bang event, while Stellar Nucleosynthesis began after the formation of the first premain-sequence stars, leading to the creation of lighter elements up to Si and to a lesser extent, heavier elements, particularly during the advanced stages of the evolution of massive stars.

In the *s*-process (slow neutron capture process), atomic nuclei are bombarded with slow-moving neutrons. The nuclei capture the neutrons, one at a time, and then decay by

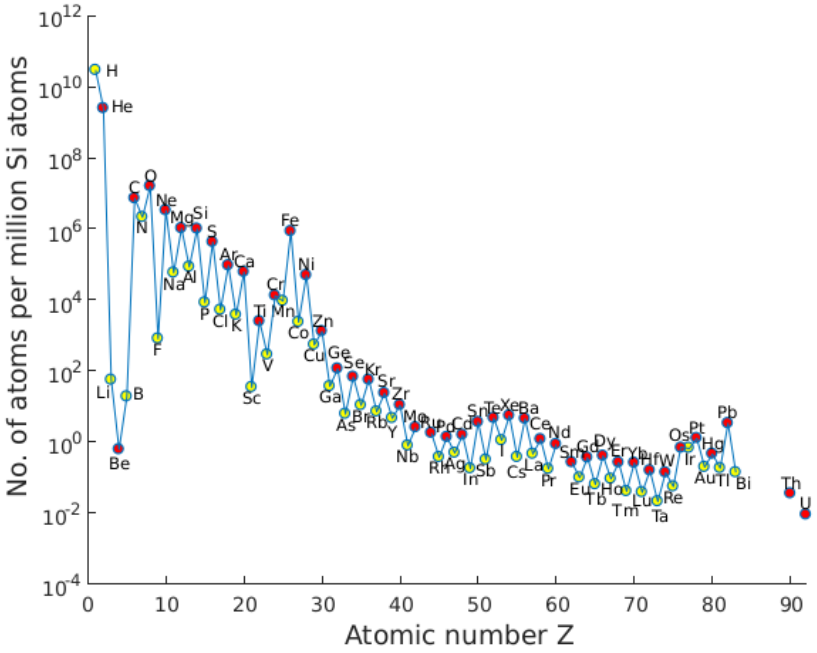

Figure 2.1: Abundances of the elements in the Solar System as a function of atomic number. The red and yellow points represents even and odd nuclei [1].

beta emission until they reach a stable configuration. This process is slow enough that unstable nuclei have time to undergo beta decay before they capture additional neutrons. The s-process mainly occurs in asymptotic giant branch (AGB) stars and results in the production of heavy elements such as lead, bismuth, and strontium.

On the other hand, in the r-process (rapid neutron capture process), atomic nuclei are bombarded with a large number of neutrons in a short period of time. This results in rapid neutron capture and the production of very neutron-rich isotopes. These isotopes are highly unstable and decay through a series of beta and alpha decays until they reach a stable configuration. The r-process mainly occurs during supernova explosions, which are the result of massive stars running out of nuclear fuel. This explosive nucleosynthesis process produces heavy elements such as gold, platinum, and uranium.

Finally, Galactic Nucleosynthesis identifies the interaction of cosmic rays with matter, producing Li and Be throughout the interstellar space. These elements serve as important tracers for the early stages of the universe and provide insight into the conditions present at the time of their creation.

2.1.1 Stellar Evolution and Nucleosynthesis

The formation of a star begins when the gravitational potential energy of the collapsing primordial cloud is transformed into thermal energy and radiation. This results in the increase in temperature and pressure that causes the first dissociation of the hydrogen molecules into atoms, along with the ionisation of hydrogen and helium atoms. Since the electrons trap radiation, the temperature and pressure rise which helps in stopping the central part of the cloud from collapsing. When the temperature reaches few million Kelvin degrees, the source of energy is not only the gravitational but also sets the first nuclear reactions occur, that is, the fusion of hydrogen nuclei to helium.

Luminosity and *temperature*, which are the quantities characterizing the star evolution, differ from star to star. The correlation of these two is represented through a plot, called *Hertzsprung-Russel* (H-R). It is a powerful tool for studying the properties and evolution of stars, allowing astronomers to classify stars based on their luminosity, temperature, and evolutionary stage. The H-R diagram reveals that stars can be grouped into several distinct regions, including the main sequence, red giants, supergiants, white dwarfs, and others, see Fig 2.2. It provides insight into the formation and evolution of galaxies, as well as the distribution and history of stars in the universe.

For example, the Sun, with a surface temperature of 5.5 mK and a luminosity of 1.0, appears yellow. Sirius A, a nearby star, is a blue-white star with a temperature of 9.94 mK and a luminosity of 23.6. Spica, a blue star of spectral type B1, has a temperature of about 22.4 mK and a luminosity of around 12,000 times that of the Sun. Betelgeuse is a red supergiant with a temperature of 3.6 mK and a luminosity of 100,000, while Rigel is a blue supergiant with a temperature of 12.1 mK and a luminosity of 85,000. Proxima Centauri, a small and faint red dwarf, has a temperature of 3.05 mK and a luminosity of 0.0017. By placing these stars on the H-R diagram, astronomers can learn more about their properties and evolutionary paths.

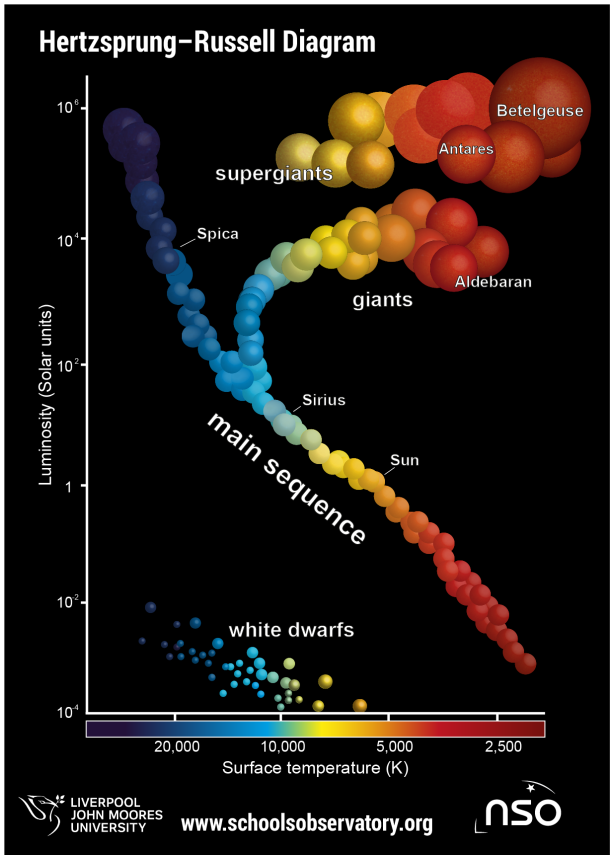

Figure 2.2: Hertzsprung-Russell diagram based on observations, displaying absolute magnitude or luminosity in relation to the sun versus color temperature or spectral class. [2].

For the stars with mass range $M/M_{\odot} = 0.1$ - 50 and a luminosity range $L/L_{\odot} = 10^{-2}$ - 10^{-6} where $M_{\odot}$ and $L_{\odot}$ are the mass and luminosity of the Sun respectively, the nuclear burning timescale for hydrogen nuclei to helium is greater and hence the majority of stars populates in the main sequence. In this stage, the conversion of hydrogen nuclei to helium is done through *proton-proton*(*pp*) chains and the *CNO* cycles. In both processes,

conversion of four ^{1}H nuclei into one ^{4}He nucleus, generates large amount of energy which is equivalent to the mass difference between the initial and final configuration. The competition between these processes are strongly dependent on star core temperature and initial composition.

The *pp* chain is dominant in primary generation stars with M 1.5 $M_{\odot}$ and a core temperature lower than 20 MK [11]. The scheme of the process as it takes place in the Sun is shown in Fig 2.3. In the pp chain, four hydrogen nuclei (protons) are fused into one helium nucleus through a series of reactions. This process releases energy in the form of gamma rays and neutrinos.

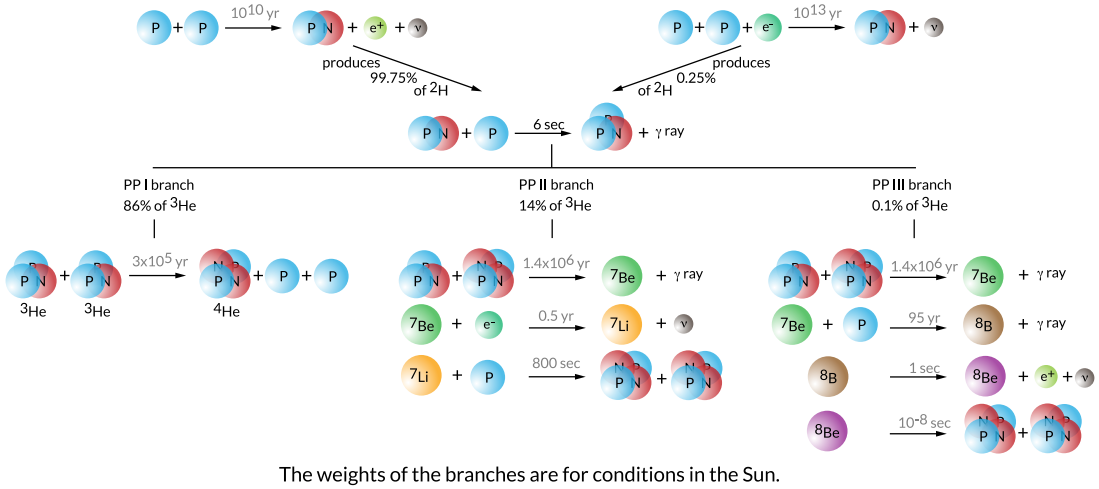

Figure 2.3: Scheme of the *pp* chain reactions, multiple chains are possible depending on the stellar temperatures [3].

The *CNO* cycle is the predominant energy generation mechanism in massive stars with core temperatures above 20 MK and masses above 15 $M_{\odot}$. This cycle is only possible if C, N and O nuclei were present in the initial protostellar nebula from which the star has been formed. As it can be seen in the Fig 2.4, it consists of four sub cycles: *CNO 1*, *CNO 2*, *CNO 3* and *CNO 4*. In all these cycles, the carbon (C), nitrogen (N), and oxygen (O) isotopes act like catalysts through proton captures and β^{+} decay in order to fuse the four hydrogen nuclei to get one helium nucleus. The cycle is less efficient than the *pp* chain but becomes more important in stars with higher temperatures and core densities. The core temperatures of stars in this cycle range from 20 MK to 40 MK, and their masses can range from 15 $M_{\odot}$to over 100 $M_{\odot}$.

After spending the majority of their lives on the main sequence undergoing hydrogen burning, stars eventually exhaust the hydrogen fuel in their cores. The timescale for this process depends on the mass of the star, with more massive stars exhausting their core hydrogen faster. Once the hydrogen burning in the core is exhausted, stars enter the Red Giant Branch (RGB) phase, which is marked by low surface temperature, high luminosity, and a mass range of $M = (0.5 - 5)M_{\odot}$ [12]. During this phase, helium begins to develop in the core, causing the hydrogen burning to move to a shell around the helium core, as shown in Fig 2.5 (left). The hydrogen burning in the shell is not enough to restrain the gravitational force, causing the core to contract and increasing the temperature and pressure. To transport the energy produced in the H-shell, a convective envelope around it is formed. This phase of the star ends when helium burning starts.

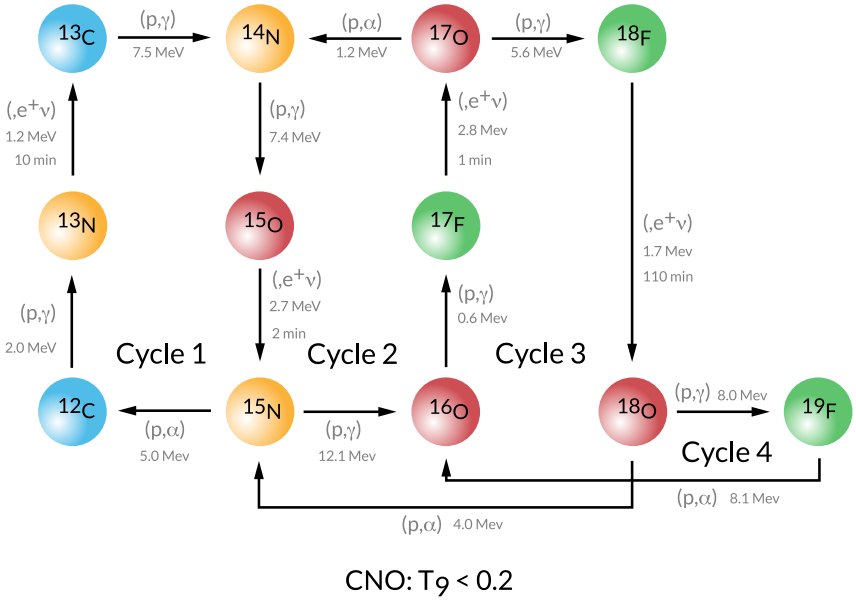

Figure 2.4: Complete scheme of CNO cycles [3].

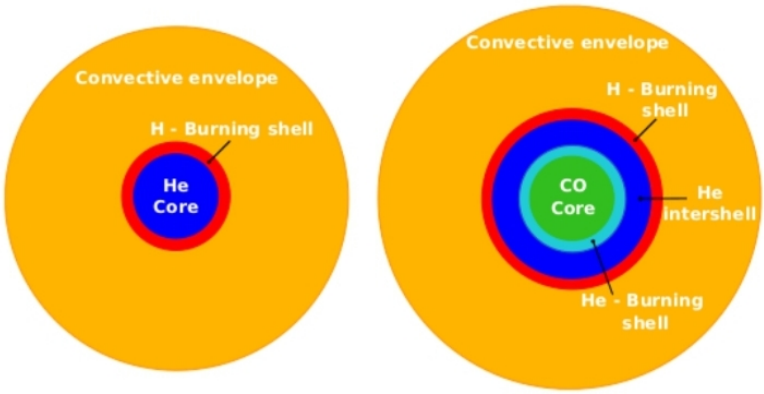

Figure 2.5: Typical structure of RGB (left) and AGB stars (right)

Next comes the Asymptotic Giant Branch (AGB) which are late-life stars with masses lesser than 10 $M_{\odot}$. In this stage, the helium burning in the core is exhausted causing the core mainly composed of carbon and oxygen, to contract again and further increasing the temperature. This process causes a helium burning transitioning to a shell which is surrounded by the hydrogen burning shell, see Fig 2.5 left. Hydrogen burning is the main source of energy of these stars, with a small part from Helium burning. The H burning occurs through periodic runway events, which releases an enormous amount of energy powering convection between the H and He shell. Once the unstable He-burning episode finishes, the base of the convective envelope is able to shrink into the intershell and this is called Third Dredge-Up(TDU). This is one of main process transporting the new synthesized materials from core to surface of the star. In these shells, helium and hydrogen burn, and a complicated interaction between the two shells isobserved [13] . The enrichment of heavierelements in the interstellar medium of AGB stars is significantly influenced by the complexprocesses in these types of stars.

After this Phase, Stars with masses less than $\sim 8\ M_{\odot}$ typically reach the end of their life cycles by becoming a white dwarf, a small and extremely dense core. However, in

more massive stars, additional burning phases occur, producing heavier elements through a process of contraction and fusion. However, the fusion burning processes eventually stop at iron and nickel nuclei, with a mass number of around 60. This is because the binding energies per nucleon start to decrease for heavier nuclei, and the fusion of nuclei to build heavier elements becomes an endothermic process. At this point, the star life cycle ends, and a supernova occurs, causing the star to explode violently. The remaining core of the star either becomes a neutron star or a black hole after the explosion, depending on the mass of the original star. The supernova explosion produces and disperses the heavy elements synthesized during the star lifetime, which can later form new stars and planets.

2.2 Thermonuclear reactions in stars

The reaction rate which is defined as the number of reactions per unit volume and time is a crucial parameter to comprehend star evolution and nucleosynthesis. The reaction $X(a,b)Y$ describes the following process:

$$a + X \longrightarrow Y + b \tag{2.1}$$

where $a + X$ is the entrance channel and $Y + b$ is the exit channel.

For a particular exothermic reaction, the energy released is represented by the Q-value. By taking energy conservation into account, the Q-value is represented as:

$$Q = (M_a + M_X - M_Y - M_b)c^2 \tag{2.2}$$

where M_a and M_X are mass of the particles in the entrance channel and M_Y and M_b are mass of the particles in the exit channel [11].

The reaction rate, r_{aX} , for this process is defined as follows:

$$r_{aX} = N_a.N_X.v.\sigma(v) \tag{2.3}$$

where N_a and N_X are the number densities of particles a and X respectively, v is the relative velocity between the two entrance channel particles, and $\sigma(v)$ is the cross-section expressed as a function of v. In a good approximation, the star plasma can be modeled as an ideal gas made up of a variety of free, non-interacting particles and because of the high temperature it can also be considered completely ionised. The relative velocities between the plasma particles is given by Maxwell-Boltzmann distribution $\phi(v)$:

$$\phi(v) = 4\pi v^2 \left(\frac{\mu}{2\pi kT}\right)^{\frac{3}{2}} exp\left(-\frac{\mu v^2}{2kT}\right) \tag{2.4}$$

where μ is the reduced mass of the two particles system, k is the Boltzmann constant and T denotes the stellar temperature. Alternatively, $\phi(v)$ can be expressed in terms of kinetic energy, E, as:

$$\phi(E) \propto exp\left(\frac{-E}{kT}\right) E \tag{2.5}$$

Having expressed this, it is now possible to define reaction rate as the following,

$$r_{aX} = N_a.N_X.\int_0^\infty \phi(v)v\sigma(v)dv = N_a.N_X.<\sigma v>_{aX} \tag{2.6}$$

where $< \sigma v >_{aX}$ is the reaction rate per particle pair. By inserting the Maxwell-Boltzmann distribution, $< \sigma v >_{aX}$ is defined as:

$$< \sigma v >_{aX} = \left(\frac{8}{\pi\mu}\right)^{\frac{1}{2}} \frac{1}{(kT)^{\frac{3}{2}}} \int_0^\infty exp\left(-\frac{E}{kT}\right) \sigma(E) E dE \tag{2.7}$$

The cross section can be expressed in terms of a quantity called the astrophysical factor S-factor $S(E)$ which contains all the essential nuclear effects in the reaction. It is given by:

$$S(E) = E\sigma(E)e^{2\pi\eta} \tag{2.8}$$

where η is the Sommerfield parameter given by:

$$\eta = \sqrt{\frac{\mu}{2E}} Z_p Z_t \frac{e^2}{\hbar} \tag{2.9}$$

where Z_p and Z_t are the projectile and target atomic number respectively, E is the projectile energy in the lab frame and μ is the reduces mass.
For the case of non-resonant reactions, the dependence of $S(E)$ on the energy is smooth and slowly varying compared to the steep dependence of cross section $\sigma(E)$ down to energy ($\frac{1}{E}$ and $exp(-2\pi\eta)$). Due to this, it is easy to extrapolate $S(E)$ on the energy region of astrophysical importance where the experimental data is not available than extrapolating the $\sigma(E)$ at these energies. In Fig 2.6, we see the dependence of $\sigma(E)$ and its corresponding $S(E)$ as a function of energy E for a typical non-resonant reaction. It can be seen that for the incoming energies less than the Coulomb barrier the cross section drops exponentially whereas the S-factor is slowly varying.

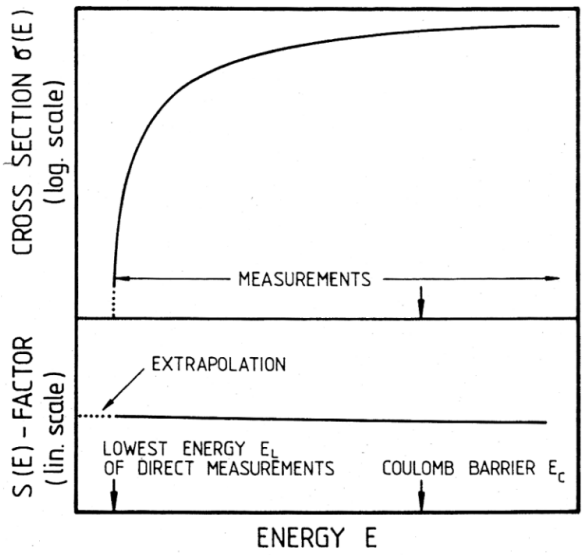

Figure 2.6: The Cross-section and the corresponding S-factor for a typical non-resonant reaction and the dotted line represents the region of astrophysical importance [4].

Now, the reaction rate $< \sigma v >_{aX}$ can be expressed in terms of $S(E)$ as:

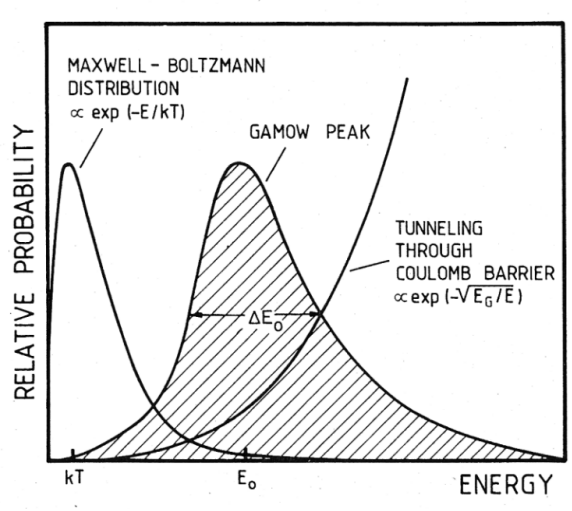

Figure 2.7: The "Gamow peak" is shown as a product of Maxwell-Boltzmann energy distribution and cross section [4].

$$\begin{aligned} < \sigma v >_{aX} &= \left(\frac{8}{\pi\mu}\right)^{\frac{1}{2}} \frac{1}{(kT)^{\frac{3}{2}}} \int_0^\infty S(E) exp(-2\pi\eta) exp\left(-\frac{E}{kT}\right) dE \\ &= \left(\frac{8}{\pi\mu}\right)^{\frac{1}{2}} \frac{1}{(kT)^{\frac{3}{2}}} \int_0^\infty S(E) exp\left(-\frac{E}{kT} - \frac{b}{E^{1/2}}\right) dE \end{aligned} \tag{2.10}$$

where the quantity b is called the barrier penetrability.

Because of the slowly varying nature of the S-factor it can be considered constant and can be taken out from the integral in equation 2.10. Then the integral is defined by the two terms: $exp(-\frac{E}{KT})$ and $exp(-\frac{b}{E^{1/2}})$. The former term is the Maxwell-Boltzmann distribution term which vanishes at high energies and the latter term is the Gamow factor describing the penetration of the projectile below the Coulomb barrier which drops exponentially at low energies. The product of these functions gives rise to the so called Gamow peak centered at E_o with width ΔE as shown in Fig.2.7. In other words, the reaction rate in 2.10 gets the most contributions from the Gamow peak region. The energy of Gamow peak E_o is much larger than $kT (E_o >> kT)$ and it is given by:

$$E_o = \left(\frac{bkT}{2}\right)^{2/3} \tag{2.11}$$

The $^{12}C(p,\gamma)^{13}N$ reaction rate, main focus of the present work, is dominated below 700keV by a broad resonance and direct capture. Experimentally, those can be treated with similar formalism since the S-factor slowly varies in the target thickness as it will be discussed in the data analysis chapter.

Chapter 3
The $^{12}C(p,\gamma)^{13}N$ reaction case

3.1 Astrophysical Motivation

The $^{12}C(p,\gamma)^{13}N$ is the first reaction in *CNO I*, as shown in Fig 2.4, which is closed by $^{15}N(p,\alpha)^{12}C$ reaction. The cycle is active during the main sequence, RGB and AGB H-shell burning. The CNO cycle not only converts four protons into one helium nucleus, but also controls the abundances of the C,N and O isotopes that participates in the cycle. The $^{12}C(p,\gamma)^{13}N$ reaction is crucial in detecting the $^{12}C/^{13}C$ isotopic abundance ratio since it depletes ^{12}C but it also produces ^{13}C through the β^+ decay of ^{13}N. The $^{12}C/^{13}C$ ratio serves as a tracer of the galactic chemical evolution since it is sensitive to stellar nucleosynthesis. However, its value is affected by the mixing process taking place in RGB and AGB stars.

In RGB stars, the $^{12}C/^{13}C$ isotopic ratio drops as a consequence of the first dredge-up [14]. On the other hand, the third dredge-up taking place in the AGB stars, shown in Fig 3.1 makes the $^{12}C/^{13}C$ ratio to increase [15, 16].

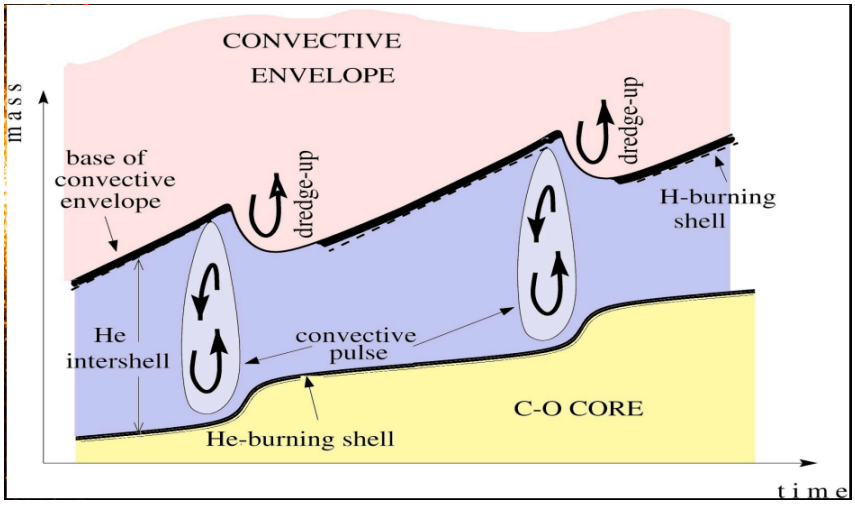

Figure 3.1: An illustration of the typical structure of AGB stars The generated elements are transported by the convective pulses across the various layers of the star, changing their abandances [5].

The CNO cycle burns at up to 100 MK degrees in H-shell burning [17]. Presently, the solar system $^{12}C/^{13}C$ isotopic ratio is thought to be around 90 [18]. The *AGB* stars [19], which are very prolific centers of nucleosynthesis, are one of the potential sources of the elements in the Solar System. To enable more accurate predictions, further knowledge of

the mixing processes taking place inside these stars is necessary as well as more precise data on $^{12}C+p$ reaction cross section.

Moreover, the $^{12}C/^{13}C$ isotopic ratios ($\approx$ 6 - 18) [7] estimated from the observation of RGB stars with the masses $M < 2.5\ M_{\odot}$ in the Milky Way and in the Magellanic Clouds is smaller than the predicted from the present *RGB* star models. The existence of novel mixing processes that are independent of the convective motion within the star is a widely accepted explanation for such a difference. The star angular momentum [20], magnetic buoyancy [21] and gravitational waves [22] are other suggested solutions. The $^{12}C/^{13}C$ ratio is also observed by analysing the SiC grains of the pristine meteorites [8]. These are produced in the atmosphere of AGB stars and should provide a identification of the composition of their progenitors.

From the discussions above it is evident the assumed rate for proton capture process on ^{12}C has a significant impact on the predicted fluctuation in the C isotopic ratio following the dredge-up events. Therefore, a precise measurement of $^{12}C(p,\gamma)^{13}N$ reaction is required to constrain the models and improve the existing knowledge on the evolution of the RGB and AGB stars.

3.2 The $^{12}C(p,\gamma)^{13}N$ reaction

The Q-value of the $^{12}C(p,\gamma)^{13}N$ reaction is 1943.5 keV and it proceeds through two resonant states located at proton energies of 457 keV and 1699 keV, see Fig 3.2. For the incoming proton energies $E_p < 457$ keV (where also the energy range for astrophysical interest is found), the reaction proceeds through a single gamma cascade γ_o by the direct capture to the ground state of ^{13}N nucleus. However for higher proton energies, the reaction proceeds through a γ_o emission to the ^{13}N ground state or to the ^{12}C ground state via a two-step process: emission of a gamma from transition to 2365 keV unbound state of ^{13}N, γ_1, and this is followed by the emission of a proton to the ^{12}C ground state. The intensities for the γ_o and γ_1 emission have been observed (92±1) % and (8±1) % at 1.7 MeV [23].

From eq.2.10, the reaction rate per particle pair for the non-resonant $^{12}C(p,\gamma)^{13}N$ reaction can be expressed as :

$$< \sigma v >_{p,12C} = 1.661 \frac{1}{(kT)^{\frac{3}{2}}} S(E_0) \int_0^{\infty} exp\left(-\frac{E}{kT} - 2\pi\eta(E)\right) dE \qquad (3.1)$$

where, 1.661 is the value of $\left(\frac{8}{\pi\mu}\right)^{\frac{1}{2}}$ calculated for reduced mass μ of p and ^{12}C at the entrance channel.

In Fig 3.3, the Gamow peak is illustrated for the $^{12}C(p,\gamma)^{13}N$ reaction in typical RGB and AGB hydrogen burning shells at temperatures of 0.03 GK and 0.1 GK respectively.

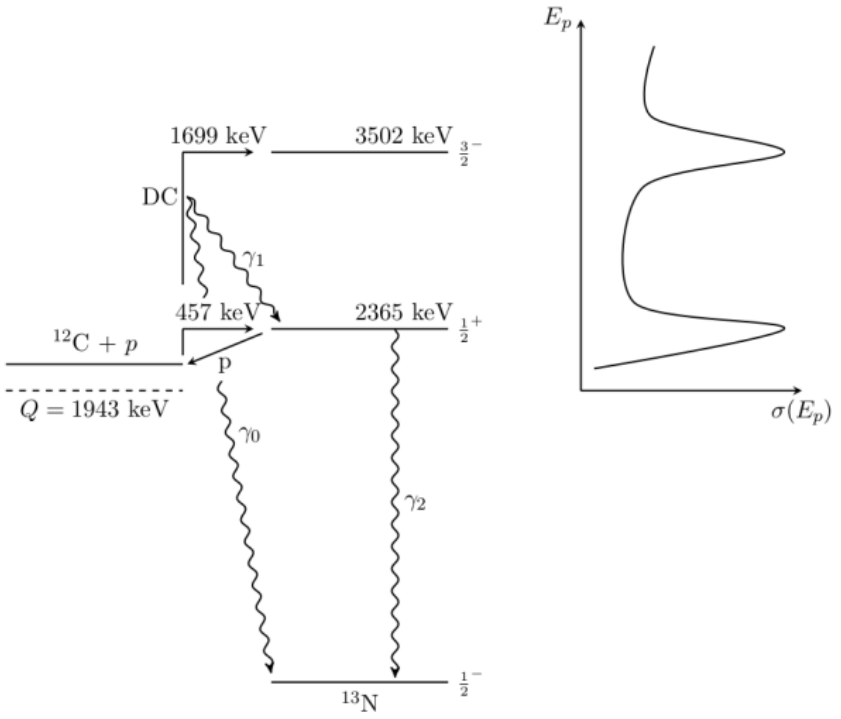

Figure 3.2: The level scheme of the ^{13}N with γ cascade for the ^{12}C(p,γ)^{13}N channel. The Q-value of the reaction is 1943.5(3).

It is clear that as the Gamow peak window lie at very low energies making the extrapolation is the only possible strategy. Thus, a precise measurement of the S-factor on a wide energy range is necessary in order to make reliable predictions about the evolution of ^{12}C abundances inside star interiors.

3.3 State of the Art

Several investigations on the ^{12}C(p,γ)^{13}N reaction have been conducted in the past over a wide energy range. Because of the reaction extremely low cross section in the Gamow peak of the RGB stars, located at about 30 keV, it is not possible to directly measure the reaction at such low energy. Therefore, the measured S-factor is usually extropolated at low energies. High precision is required to achieve a reliable result because the extrapolation process is very susceptible to measurement errors. On the contrary, experimental data are available in the Gamow window for AGB stars.
In the following, the previous measurements of the reaction are presented, the data are shown in Fig 3.4:

1. In 1949, Baily [24] and Hall et al. [25] conducted two tests at the same time for two distinct energy ranges. Using a thick carbon target (graphite), the former measured the ^{12}C(p,γ) ^{13}N cross section between 125 and 200 keV. The latter experiment covered the 88 keV to 128 keV energy range. In both cases, the environmental background could not be entirely suppressed, making impossible to directly identify the prompt γ-ray at such low energies. Thus, the activation technique was employed. The total cross section error was estimated to be roughly $\pm$ 20%.

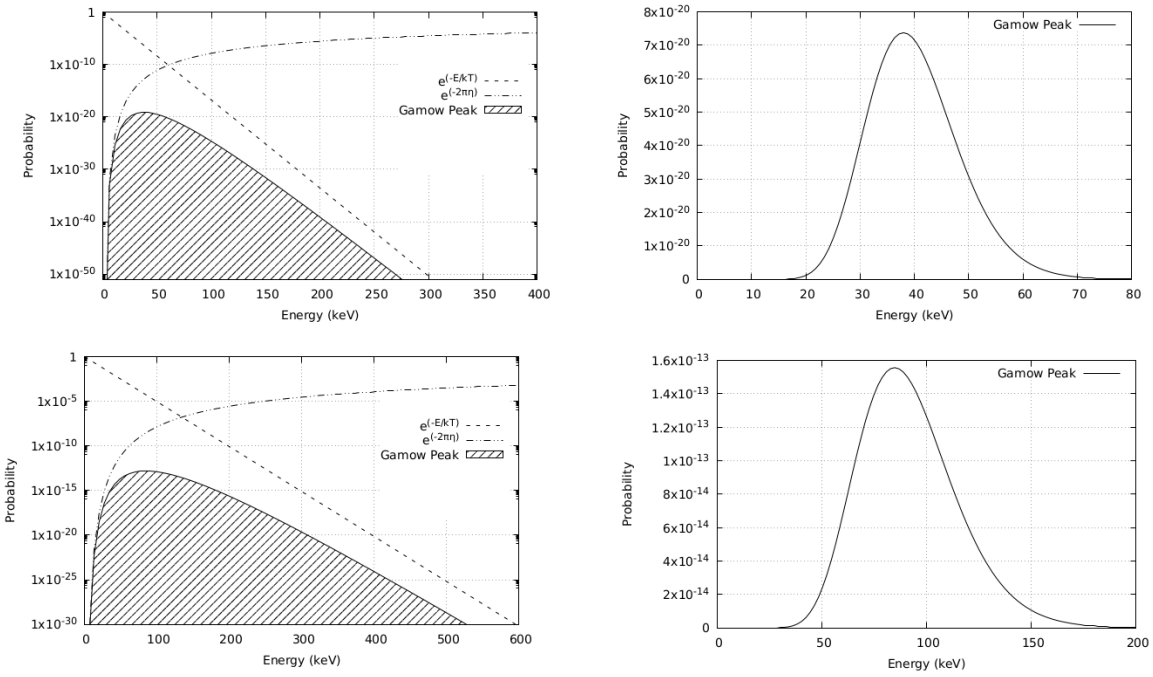

Figure 3.3: The Gamow peak (filled region) for the $^{12}C(p, \gamma)^{13}N$ reaction was computed with T = 0.03 GK (*RGB* star)(Top left) and was computed with T = 0.01 GK (*AGB* star)(Bottom left) . The dashed lines on the graph represent the two contributions. The second plot shows, the Gamow peak of both stars in linear scale.

2. In 1957, Lamb et al. [26] reported a measurement of the $^{12}C(p,\gamma)$ ^{13}N reaction cross section at energies between 80-126 keV. The analysis focused on the transition to the ground state of ^{13}N and the analysis was susceptible to background noise since the same energy window for the γ-spectrum was used for all energies. The measurements are affected by errors which ranges from $\pm$13% to $\pm$41%.

3. In 1963, J. Vogl [27] investigated the reaction for his PhD thesis, data were not published. A 150 keV to 680 keV energy window range was investigated. Though the results obtained are in good agreement with the previous experiment, the cross section error at low energies ($<$ 230 keV) was considerably high (20% to 90%).

4. In 1974, the $^{12}C(p,\gamma)^{13}N$ reaction was examined by Rolfs et al [28]. Even if, the two ^{13}N excited states at 2365 keV and 3502 keV were the main focus of the experiment, the cross section was measured at proton energies as low as 150 keV. The measurement was performed with detector placed at both 0 and 90 degrees and the uncertainity was of 14%. The extrapolation of the produced S-factor results is in good agreement with the previously cited works.

5. Recently $^{12}C(p,\gamma)^{13}N$ reaction was also studied by Burtebaev et al. in 2008, [29]. New measurements of differential and total cross sections have been measured at different beam energies in the energy range E_p = 350 - 1061 keV.

With the exception of the data from Fowler et al., which are not included in any database, all the different literature data are compared in Fig 3.4. Since the data were initially presented as a cross section, Equation 2.8 was used to convert the points into S-factors. The Gamow window for RGB is still largely unexplored, as seen in Fig 3.4. Furthermore,

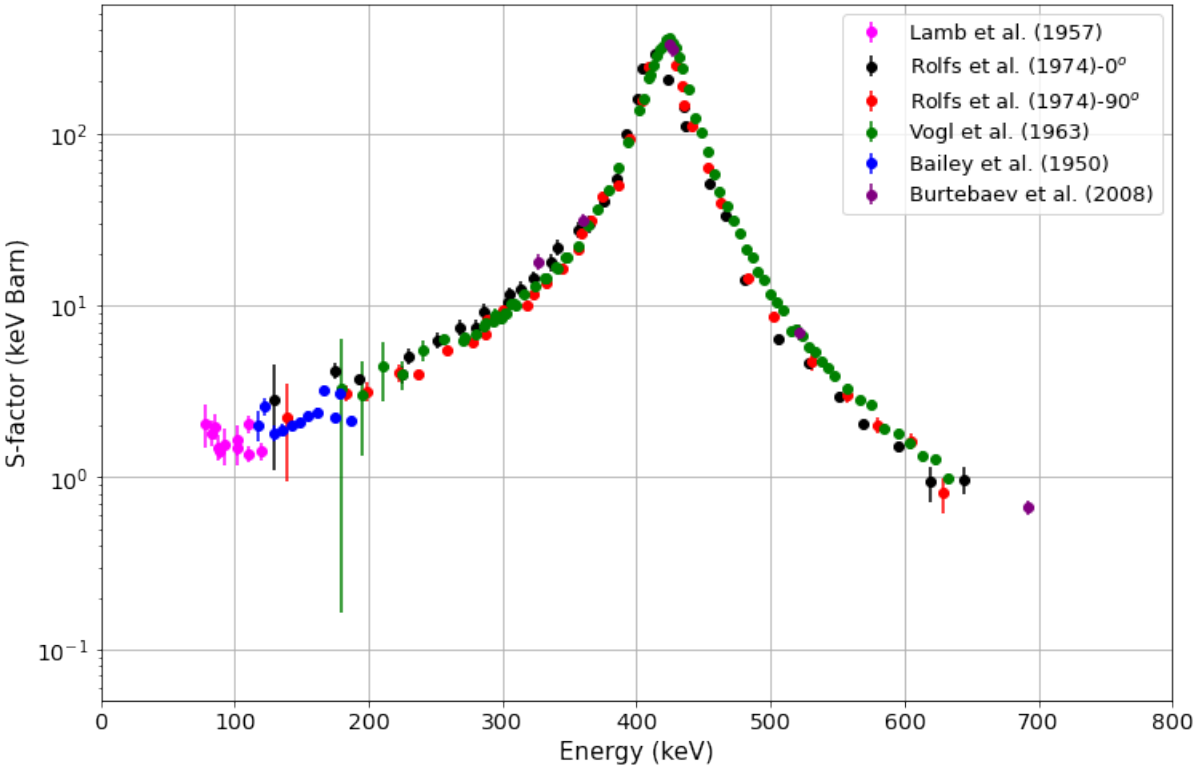

Figure 3.4: Comparison of S-factor results for $^{12}C(p,\gamma)^{13}N$ reaction for most of the literature data.

there is little energy overlap among the various data sets. There is however a discrepancy for the lower energy resonance E_r observed in $^{12}C(p,\gamma)^{13}N$ reaction since E_r reported by Rolfs et al [28] is 421±1 keV whereas it was found to be 426±2 keV by Vogl et al in [27]. It was also reported in [27] that the calculations made with E_r=421 keV is outside the data uncertainity. A recent measurement in 2008 by Burtebeaev et al. [29] still does not solve this discrepancy due to the few data points reported.

Chapter 4
Experimental Setup

The study of $^{12}C(p,\gamma)^{13}N$ reaction was performed using 5MV pelletron accelerator at Felsenkeller shallow Underground facility, Dresden (Germany). The beam transmission is optimised by using a number of focusing and collimating elements installed on the beamline. The scattering chamber and the target holder were adapted to minimise the target degradation and to precisely measure the beam current. An High Purity Germanium (HPGe) cluster detector, placed in close geometry as used to detect the γ-rays from the $^{12}C(p,\gamma)^{13}N$ reaction. Four additional detectors were placed at different angles and in far geometry to check the angular distribution. In the following sections, a detailed description of the experimental setup is reported.

4.1 Felsenkeller shallow underground facility

For charged-particle-induced reactions, the cross section $\sigma(E)$ drops exponentially at the energies of astrophysical interest which are below the Coulomb barrier. Moreover the study of reactions at these energies is a hard task since the background radiation compete with the reaction signal. The sources of background radiation are multitude. The main type is the radiation caused by cosmic rays. Cosmic rays which are mainly constituted of high energy protons and alpha particles can produce muons when passing through the Earth atmosphere. Muons are highly penetrating particles and also can interact with other particles and nuclei producing neutrons and gamma rays affecting the detection of gamma ray signal coming from the actual nuclear reaction. The cosmic ray background is reduced by order of magnitude at Felsenkeller facility since the experiments are conducted under 45 m of rock which acts as a natural shielding [6]. Another source of background radiation arises from the radionuclides present in the rocks and materials surrounding and inside the laboratory. Several experiments were conducted to measure the background γ radiation in the underground Felenskeller facility and was compared with the values obtained at Earth surface using HPGe detectors. Fig 4.1 shows the γ spectra recorded by one HPGe detector, HZDR-2 (60 % HPGe), which was placed at Earth surface and in two different underground locations: tunnel VIII and tunnel IV of Felsenkeller facility [30]. It can be clearly seen from figure that for gamma energy $E_\gamma < 3$ MeV, the background radiation is dominated by the radionuclides ^{40}K ,^{238}U and ^{232}Th present in the rock. This contribution can be reduced by adding passive or active shielding all around the detector. For gamma energies above 3.5 MeV, the background radiation count is highly suppressed compared to the counts observed in overground laboratories.

The γ-ray background radiation due to cosmic ray and radionuclides present is referred as the environmental background. In addition to this, there is a significant contribution to

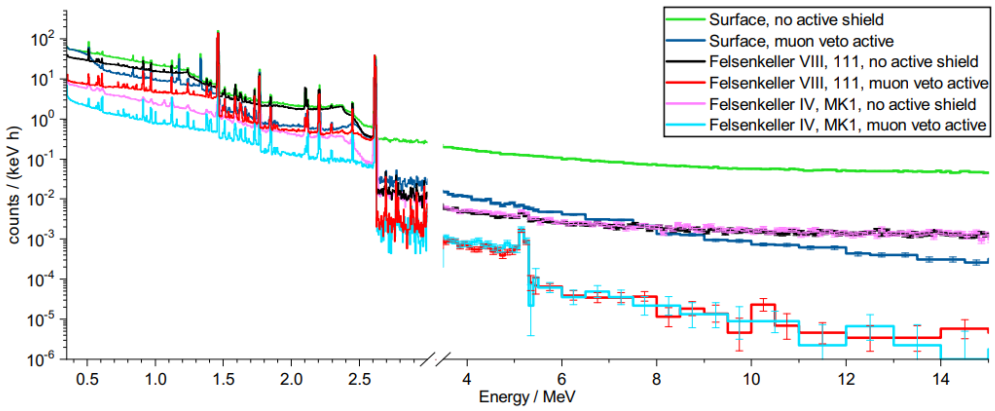

Figure 4.1: The γ-ray energy spectra recorded with detector HZDR-2 (60% HPGe) at Earth's surface, underground at Felsenkeller tunnel VIII, room 111, and at Felsenkeller tunnel IV, MK1. [6]

the background from the so called beam induced background. The solid ^{12}C target used to study ^{12}C(p,γ)^{13}N reaction contained 1% ^{13}C nuclei. Due to this, there was a beam induced background observed mainly through Compton by the ^{13}C(p,γ)^{14}N resonance at $E_p = 604$ keV.

4.2 The 5 MV pelletron accelerator

At the Felsenkeller facility, a 5 MV Pelletron tandem accelerator of type 15SDH-2 produced by National Electrostatics Corporation (NEC), USA is installed. The accelerator has been located inside the connecting tunnel between tunnels VIII and IX of the Felenskeller underground facility, see Fig. 4.2.

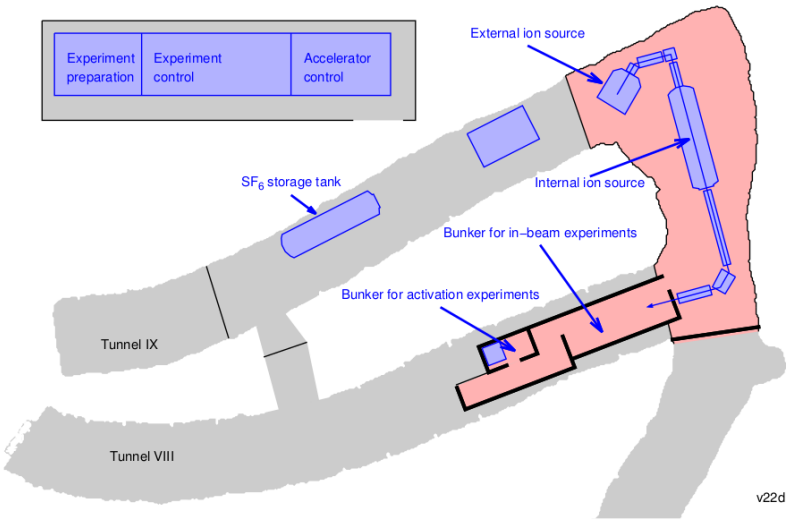

Figure 4.2: Layout of the Felsenkeller accelerator laboratory in tunnels VIII and IX.

The 5 MV pelletron accelerator has two different ion sources. First one is the external cesium sputterring ion source of type 134 MC-SNICS developed by NEC and it can provide up to 100 μA ^{12}C$^-$ beam [30]. The second one is an internal radio frequency (RF) ion

source which was also made by NEC. Mounted on the high-voltage terminal behind a custom-made electrostatic deflector, this ion source has the possibility of working in both tandem and single-ended modes. In tandem mode, heavy mass particles like C, N ,O can be accelerated while in a single ended mode light mass ions like H or He are provided by the 5MV Pelletron accelerator. It was found that that RF ion source can deliver up to 90 μA $^4He^+$ beam. Because of this distinctive combination a variety of hydrogen and helium burning processes that occur in the stars can be investigated. For the present $^{12}C(p,\gamma)^{13}N$ experiment, the pelletron was used in single-ended mode providing ≈ 10 μA of H_2^+ beam. A ≈ 1 μA proton beam was also provided for the target characterisation and efficiency measurement.

4.3 The Scattering Chamber

The well collimated proton H_2^+ beam reaches the target with a final diameter of 5 mm. The energy range covered by the molecular beam was 350 - 700 keV, while proton beam were used for efficiency and target monitoring aims. Both the scattering chamber and the target are insulated from the beamline, thus they act as a Faraday cup allowing the direct reading of beam current directly during each measurement. Secondary electrons are produced due to the interaction of the beam particles with the target. These electrons escape from the target and cause incorrect current reading. In order to suppress the secondary electrons, a copper tube was installed inside the chamber, at a distance of 20 mm from the target. A negative potential of 200 V was applied to the copper tube, to deflect electrons emitted from the target back onto it. The scattering chamber and the target beamline were both isolated from the copper tube. Additionally, the copper tube was used as a cold finger during the measurement to avoid carbon buildup on the target. This was achieved by keeping the copper tube in thermal contact with LN2.

4.4 The Target

Target was mounted at 0 degree with respect to beam direction and it was cooled in order to limit target degradation. The target was indeed in thermal contact with $LN_@$ dewar (see Fig 4.4). For the present work, two targets of slightly different thicknesses were irradiated and are listed in Tab 4.1

The targets were produced at ATOMKI Laboratories, Hungary, by evaporating natural carbon powder consisting of 99% ^{12}C and 1% ^{13}C on tantalum backlings 27 mm diameter and 0.2 mm thick previously cleaned by acid and ultrasonic baths, and mechanical processes.

The evaporation was performed by the electron gun technique using a Leybold UNIVEX 350 vacuum evaporator at ATOMKI. The natural ^{12}C powder is put into a copper melting pot which is heated using an electron gun. An adjustable arm is used to hold the tantalum disk at 10 cm from the melting pot in order to obtain a uniform deposition layer. To monitor the evaporation, an oscillator quartz was mounted inside the vacuum chamber , which can measure the thickness of the deposition online [31]. The evaporation procedure can cause changes to the target composition, and the nominal target thickness calculated using evaporation parameters is subject to significant uncertainty. Due to these

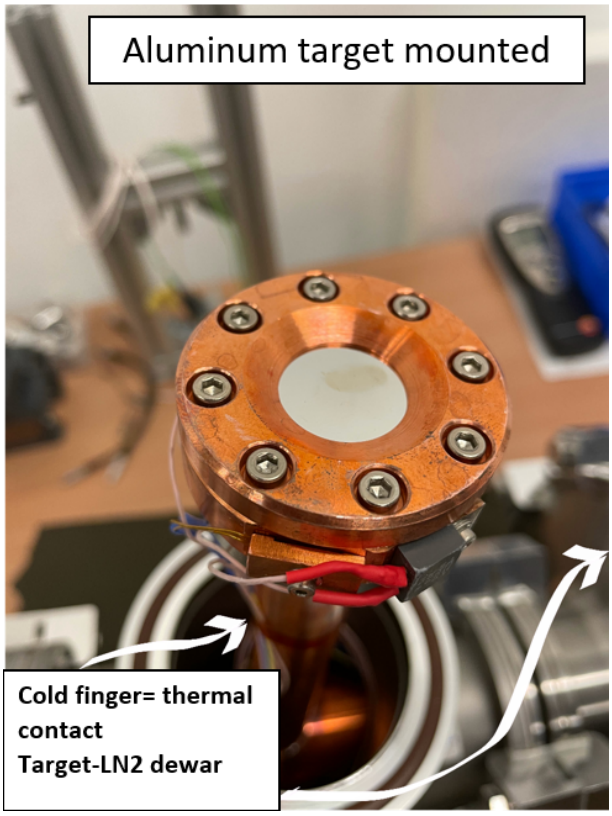

Figure 4.3: Target holder connected to LN2 pipe through cold finger, to reduce heating from the beam.

factors, the target thickness and composition are typically determined through devoted experiments. The methods used for target characterisation are described in later sections.

Target name	Nominal Thickness NRRA	Nominal Thickness (Atoms/cm^2)
T12C_L1	∼4 keV	1243
T12C_L4	∼5.5 keV	1803

Table 4.1: List of the targets used for the current study with their nominal thickness as reported by producer.

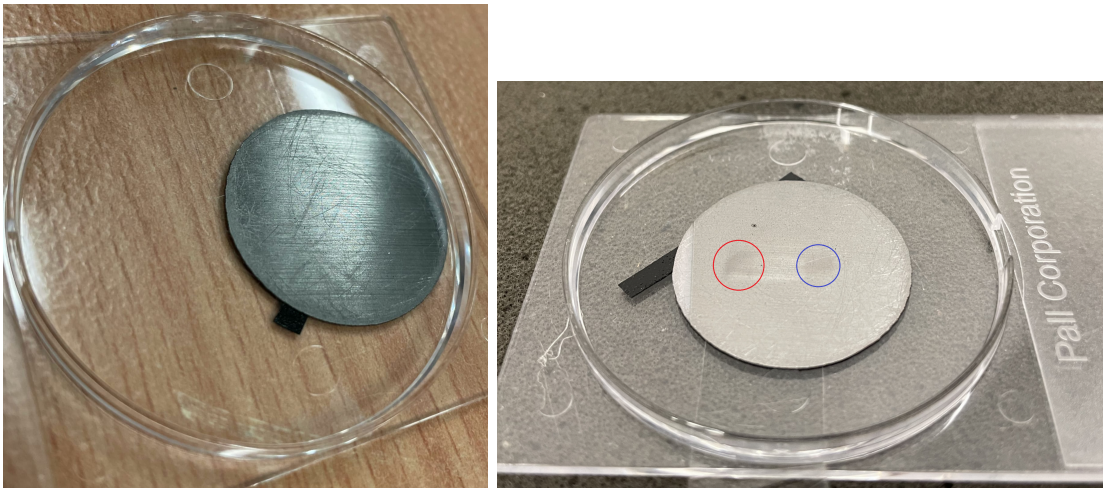

Figure 4.4: Pictorial comparison of the target before (left) and after (right) the irradiation of the proton beam. Beam spot 1(red circle) and beam spot 2(blue circle) are two beam spots shown on the irradidted target.

4.5 Detectors and DAQ

4.5.1 HPGe Detector

An HPGe detector was used to detect the γ rays coming from ^{12}C(p,γ)^{13}N reaction experiment that was performed at the Felsenkeller facility. The HPGe detectors are based on the principle of semiconductive properties of germanium (Ge). Due to its low band gap (0.7 eV), Ge can give rise to a high number of charge carriers (electron-hole pairs) and is hence helpful in determining the intensity of the incoming photon radiation to a good extent. In addition to this, the energy resolution of the HPGe detectors is high, for example, the energy resolution was found to be around 2 keV at gamma energy E_γ=1.3 MeV as reported in [32]. However, due to the limited size and low atomic number of Ge, the efficiency of an HPGe detector is low for energies $E_\gamma > 1$ MeV when compared with scintillators [32]. In the ^{12}C(p,γ)^{13}N experiment performed at Felsenkeller, the efficiency of HPGe is not a major problem since the expected gamma count rate is high, while the high resolution is a required feature since the γ-peak from the reaction of interest lays very close to background and beam induced background.

The solid target used in studying this reaction was surrounded in total by 5 HPGe-cluster detectors as shown in Fig. 4.5, namely MB1, MB2, EB17, EB18, and a single crystal detector Can60. The number of HPGe detectors in each cluster and their angular and spatial orientation from the target is summarised in Table 4.2. The scheme of all detectors is shown in Fig. 4.6.

Figure 4.5: The experimental configuration during the measurement.

Detector name	No. of HPGe crystals	Angle (in degrees)	Distance (in cm)
MB1	3	122	39.0
MB2	3	55	37.5
EB17	7	90	1.7
EB18	7	114	14.4
Can60	1	22	17.1

Table 4.2: Details of 5 HPGe cluster detectors used in the study of ^{12}C (p,γ) ^{13}N reaction .

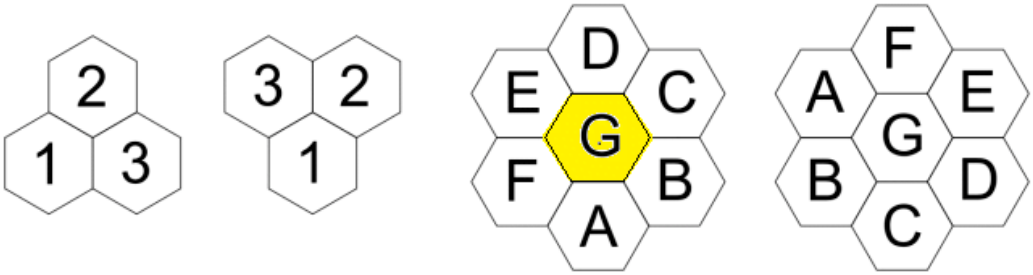

Figure 4.6: Scheme of all the detectors in the following order : MB1, MB2, EB17, EB18. Data from the highlighted detector were used in the present work.

In this current work, data analysis was performed only for the central HPGe detector G in cluster EB17.

4.5.2 DAQ

A scheme of the Data Acquisition chain for a single crystal used for the current measurement is shown in Fig.4.7. We used five HPGe cluster detectors, each with a different number of HPGE detectors, as mentioned in the section before. The five-detector signal is split into two digitizers with different gains (DAQ 1 and DAQ 2). Table 4.3 displays the two DAQ schemes. The scheme of both the DAQ are identical, apart from this DAQ 1 has an additional signals channel for Copper charge and Target charge is essential for the analysis.

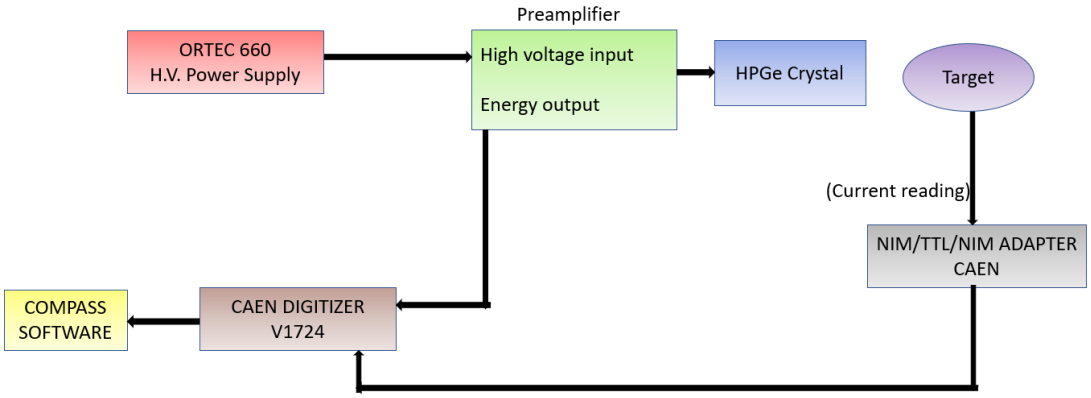

Figure 4.7: Schematic representation of Data Acquisition System.

The ^{12}C (p, γ) ^{13}N reaction peak was detected at approximately channel number 2100 in the DAQ2 and at channel number 7300 in DAQ1.

Data Acquisition is carried out until counting statistics $\sim$ 10000 counts in the MB1 and MB2 detectors because of their low efficiency. In case of low counting rates, the statistics are checked in EB17-18 detectors and at least one of these should have 10000 counts.

Board 179							
Detector Channel	EB17/A 1	EB17/B 2	EB17/C 3	EB17/D 4	EB17/E 5	EB17/F 6	EB17/G 7
Detector Channel	MB1/1 10	MB1/2 11	MB1/3 12	MB1/BGO 13			

Board 397								
Detector channel	EB18/A 0	EB18/B 1	EB18/C 2	EB18/D 3	EB18/E 4	EB18/F 5	EB18/G 6	
Detector Channel	EB18/BGO 7	MB2/1 8	MB2/2 9	MB2/3 10	MB2/BGO 11			
Signal Channel	Copper Charge 12	Target Charge 14						

Table 4.3: DAQ 1 and DAQ 2 channel map.

Chapter 5
Data analysis and results

The data acquisition took place during spring 2022 and it was structured as following: Efficiency calibration of HPGe detectors was performed using standard calibration sources and ^{27}Al(p,γ)^{28}Si reaction. Then we moved to ^{12}C targets, the first target (T12C_L1) has a nominal thickness of 4 keV. It was first characterized through resonance scan of ^{13}C(p,γ)^{14}N resonance at 1748 keV. Thereafter, a measurement was performed at 380 keV as the reference energy to have an additional target monitor during the measurement. Then the measurement of the ^{12}C(p,γ)^{13}N reaction cross section was performed in a wide energy range, from 350 to 700 keV in steps of 10 keV. Periodically, we performed a run at 380 keV to check that the yield is consistent with the first 380 keV run (see Fig.5.1). At the end of the measurement for the T12C_L1 target, a second resonance scan was also performed.

Experimental measurements for the second target (T12C_L4) (5.5 keV nominal thickness) were also performed by following the same steps as for the first target, except for the second resonance scan because of time constraints. The measurement was performed with target of different thickness in order to check the possible systematics coming from target.

5.1 Yield and Cross section

The *reaction yield* is the quantity we have access to when performing direct measurements and it is defined as the ratio of the total number of reactions, N_R over the total number of incident beam particles, N_b. Experimentally, total yield is given by:

$$Y = \frac{N_R}{N_b} = \frac{N_\gamma}{N_p \eta_{ph}(E_\gamma) W(\theta) B_r} \tag{5.1}$$

where N_γ is the number of observed gamma rays in the region of interest, N_p is the number of incoming protons, B_r is the branching ratio of the γ-ray transition, $\eta_{ph}(E_\gamma)$ is the detector efficiency and $W(\theta)$ is the angular distribution.

The ^{12}C (p,γ) ^{13}N reaction proceeds through a single gamma cascade γ_0 at $E_p < 457$ keV, by the direct capture to ground state. At higher proton energies, the reaction either returns to the ^{12}C ground state in two steps—emitting a gamma from the transition to the 2365 keV unbound state of ^{13}N, γ_1, and then emitting a proton to the ^{12}C ground state or it proceeds to the ^{13}N ground state in a single gamma emission,γ_0. According to [28], the observed intensities of γ_0 and γ_1 are (92 $\pm$ 1)% and (8 $\pm$ 1)%, respectively

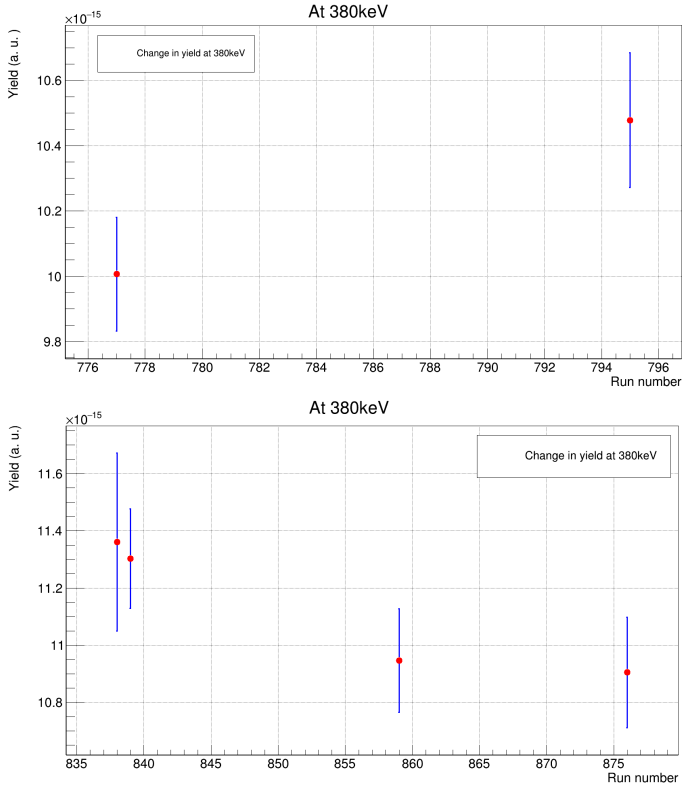

Figure 5.1: Yield of the ^{12}C (p,γ) ^{13}N reaction required with E_p=380 keV with respect to Run number, first plot refers to T12C_L1 target and second plot refers to T12C_L4. The yield is in good agreement.

at 1.7 MeV. The latter, however, was found to be 5% in a previous measurement [23]. Additionally, there is no additional data available for the gamma cascade in the literature cited in the second chapter. Therefore, we assumed that at Ep = 457 keV, only a single gamma is emitted during the ^{12}C (p,γ) ^{13}N reaction. This assumption was made due to the lack of experimental evidence to suggest otherwise. It is important to note that any future experimental data may require a reassessment of this assumption. For the present analysis the γ_1 was observed. Additionally, it is assumed that the γ-ray angular distribution is isotropic, so $W(\theta) = 1$ as expected by theory and as found in [28], see Fig. 3.4. At resonance energy, $E_p = 457$ keV, a single gamma(γ_2) is emitted corresponding to de-excitation of $E_x = 2364.9(6)$ keV level.

The total yield Y can also be expressed in terms of the reaction cross section, $\sigma(E)$, [11]:

$$Y = \frac{N_R}{N_b} = \int_{E_0-\Delta E}^{E_0} \frac{\sigma(E)}{\epsilon_{eff}(E)} dE \tag{5.2}$$

where $\epsilon_{eff}(E)$ is the effective stopping power and it accounts for the number of active nuclei in the target, ΔE is the total energy lost by the beam in the target and E_0 is the incident beam energy.

We can obtain the cross section by determining the experimental yield, effective stopping power, and the target thickness. More specifically, the S-factor is the quantity we are

interested:

$$Y = S(E) \int_{E_0-\Delta E}^{E_0} \frac{exp(-2\pi\eta(E))P(E)}{E\epsilon_{eff}} dE \tag{5.3}$$

where we use eq.2.8 to define the cross section in eq. 5.2, and $P(E)$ is the normalized target profile.

The aim of our experiment is to calculate the S-factor for the ^{12}C (p,γ) ^{13}N reaction. The experimental yield can be expressed as:

$$Y_{(p,\gamma)} = S_{(p,\gamma)}(E_{cm}).\eta_{ph}. \int_{E_p-\Delta E}^{E_p} \frac{e^{-2\pi\eta}.P(E).W(\theta,E)}{\epsilon_{eff}(E)E_{cm}} dE \tag{5.4}$$

where S-factor $S_{(p,\gamma)}$ is considered almost constant over the target thickness ΔE, η_{ph} is the full peak efficiency of the detector, $P(E)$ is the target profile at each proton energy E_p, $\epsilon_{eff}(E)$ is the effective stopping power of ^{12}C for proton at energy E_p, and $W(\theta,E)$ is angular distribution co-efficient which is 1 in our case since the present reaction is isotropic.

The S-factor can be calculated by re-writing the Equation.5.4 as:

$$S_{(p,\gamma)}(E_{eff}) = \frac{Y_{(p,\gamma)}}{\eta_{ph}. \int_{E_p-\Delta E}^{E_p} \frac{e^{-2\pi\eta}.P(E).W(\theta,E)}{\epsilon_{eff}(E)E_{cm}} dE} \tag{5.5}$$

Where $S(E_{eff})$ is the astrophysical S-factor at the *effective energy*, E_{eff}, which is defined as:

$$E_{eff} = \frac{\int_{E_0-\Delta E}^{E_0} E\sigma(E)dE}{\int_{E_0-\Delta E}^{E_0} \sigma(E)dE} \tag{5.6}$$

E_{eff} is the effective energy in the laboratory reference frame. The transformation from the laboratory frame, E_{lab} to Center of Mass frame, E_{cm} in a two body collision is:

$$E_{cm} = E_{lab}\frac{m_2}{m_1+m_2} \tag{5.7}$$

where m_1 and m_2 are the masses of the projectile(p) and target(^{12}C) nuclei, respectively.

Each component of the eq.5.5 to calculate the S-factor is explained in following sections.

5.2 Stopping Power

When a charged particle passes through a certain material, it slows down by losing a part of its energy primarily due to the inelastic collisions with atomic electrons. The rate of energy loss is referred as *linear stopping power*,$\epsilon_{lin}(E)$:

$$\epsilon_{lin}(E) = -\frac{dE}{dx} \tag{5.8}$$

where dE is the infinitesimal energy loss in the infinitesimal spatial distance dx.
The stopping power is usually expressed in terms of the energy loss per unit areal density, ρ (typically given units of atoms per cm^2):

$$\epsilon(E) = -\frac{1}{N}\frac{dE}{dx} \tag{5.9}$$

where N is the number density (atoms per cm^3) of the target material.
Theoretical explanation of charged particles interacting with matter is more complex. But, the Bethe formula [32] provides a good approximation of the energy loss of the charged particle passing through matter at high energies:

$$\frac{dE}{dx} = \frac{4\pi e^4 z^2}{m_e v^2} NB \tag{5.10}$$

where

$$B = Z\left[ln\left(\frac{2m_e v^2}{I}\right) - ln\left(1 - \frac{v^2}{c^2}\right) - \frac{v^2}{C^2}\right] \tag{5.11}$$

Above equation describes the theoretical stopping power for a projectile of charge z with velocity v passing through a medium composed of element with atomic number Z. I represents the ionization potential, and m_e the mass of electron. The stopping power is inversely proportional to the energy (as $E \propto v^2$), and the energy loss is directly proportional to the charge of both projectile and target.

Until now, it was considered that the targets were only composed of one element. This is obviously not the case in many nuclear physics investigations. Typically, the target is constructed from a variety of materials. Additionally, it is necessary to consider the existence of contaminants. In this case, *Effective stopping power* is used which is related to the number of active nuclei in the target and calculated as [4]:

$$\epsilon_{eff} = \epsilon_a + \Sigma_i \frac{N_i}{N_a}\epsilon_i \tag{5.12}$$

where N_a are referred as *active* nuclei and N_i are the *inactive* nuclei present in the target, those not involved in the reaction of interest, but takes part in slowing down the projectile,and ϵ_a and ϵ_i are the stopping power for active and inactive nuclei respectively. In the present experiment, the effective stopping power is given by:

$$\epsilon_{eff}(^{12}C) = \epsilon(^{12}C) + \frac{N(^{13}C)}{N(^{12}C)}\epsilon(^{13}C) \tag{5.13}$$

Where the ^{12}C and ^{13}C are the active and inactive respectively present in the target (percentage of ^{13}C is explained in target composition). The stopping power of both C isotopes are the same, so the eq.5.13 can be simplified as:

$$\epsilon_{eff}(^{12}C) = \epsilon(C) \tag{5.14}$$

SRIM [33] is a computer coded software, which is very helpful in calculating the stopping power of the projectile for different target-projectile systems at various incoming projectile energies. However, SRIM does not provide the stopping power values for all energies, so a linear interpolation has to be performed to calculate stopping power at certain energies. For the required ^{12}C (p,γ) ^{13}N reaction, the stopping power for ^{12}C nuclei as a function of proton energy is presented in Fig 5.2.

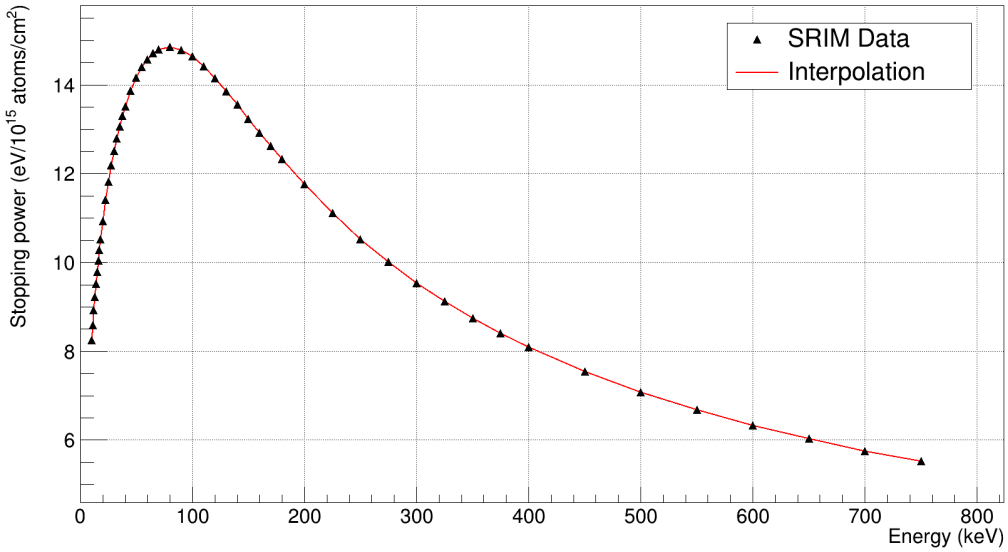

Figure 5.2: Stopping power for protons inside the carbon target using SRIM software.

5.3 Efficiency

The efficiency calibration for the experimental setup was performed using pointlike calibration sources, ^{137}Cs and ^{60}Co, and the γ-rays from the well known ^{27}Al(p,γ)^{28}Si resonance at $E_p = 994.4$ keV [34]. The ^{88}Y source was also acquired but it was not included in the efficiency calibration because the geometry was different.

For $E_\gamma < 2000$ keV, the efficiency calibration was fixed just using the calibration sources, ^{137}Cs and ^{60}Co. ^{137}Cs nuclei decays through a single γ-ray of 662 keV. The ^{60}Co nuclei decays with 99% probability to 2507 keV level of ^{60}Ni via β^- decay, and then emitting two different γ-rays in cascade: the primary at 1173 keV and the secondary at 1332 keV. Both sources were mounted on a target holder in the same way as the targets.

The absolute full-energy peak efficiency is defined as the ratio of the measure peak area to the number of γ-rays emitted by the radioactive nuclide in the whole solid angle. It can be calculated using the equation:

$$\eta_{ph} = \frac{N_{counts}}{A\Delta t Br} \tag{5.15}$$

where N_{counts} is the number of counts inside the γ-peak of interest, Δt is the measuring

Sources	Gamma energy (keV)	Efficiency(%)	Efficiency error(%)
^{60}Co	1173.238(3)	0.3325	0.0025
^{60}Co	1332.502(4)	0.3152	0.0023
^{137}Cs	661.636(3)	0.3946	0.0088
^{27}Al(p,γ)^{28}Si resonance	10762.900	0.0546	0.0050

Table 5.1: List of efficiency and its errors for the calibration sources and $E_\gamma = 10.762$ MeV from 994.4 keV resonance of the ^{27}Al(p,γ)^{28}Si reaction

time of the experiment and Br is the branching ratio of the emitted γ-ray, and A the activity of source at the measurement time.

5.3.1 Efficiency Calibration with ^{27}Al(p,γ)^{28}Si reaction

The present Region of Interest lies in the range 2-3 MeV. In order to extend the efficiency calibration beyond E_γ=2 MeV,the ^{27}Al(p,γ)^{28}Si resonance at E_p = 994.4 keV was exploited. The γ-rays from the 12.5795 MeV level de-excitation ranges from 1.5 - 11MeV [34], giving an opportunity to check the detector response in a very wide range of energy. Because of the low statistics we used only one γ-ray with $E_\gamma = 10.7629$ MeV for the efficiency calibration. This is the prominent γ-ray (Br = 76.6 $\pm$ 1.5)% [34] which corresponds to 12.5795 MeV excited level decays to 1778.9 keV state.

The efficiency was calculated using the equation :

$$\eta_{ph} = \frac{Y_{th.}}{Y_{exp.}} \tag{5.16}$$

where $Y_{exp.}$ defined by the ratio between the total number of nuclear reaction, N_R that occurred and the total number of incident beam particles, N_p using 5.1. The total $Y_{expt.}$ has to be divided for the branching ratio of 10.762 MeV γ-ray, Br = (76.6 $\pm$ 1.5)%. N_p is calculated as Q/e, where Q is the total charge accumulated on target and e is the charge of the electron.

The $Y_{th.}$ is defined in the case of a single narrow resonance at $E = E_{res}$, and an infinitely thick target [11] as:

$$Y_{max,\Delta E\to\infty} = \frac{\lambda_{res}^2}{2}\frac{\omega\gamma}{\epsilon(E_{res})} \tag{5.17}$$

Where $\epsilon(E_{res})$ is the effective stopping power at resonance energy(E_p = 994.4 keV) which is calculted using SRIM [33], $\omega\gamma$ is the resonance strength for resonance energy in the Center of Mass(E_{CM} = 956.548 keV), the value is taken from [35] ($\omega\gamma = 1.19(11)$)and λ is the de Broglie wavelength in the Center of Mass which is calculated numerically as:

$$\frac{\lambda^2}{2} = \left(\frac{m_p + m_T}{m_T}\right)^2 \frac{4.125 * 10^{-18}}{m_p E_\gamma^{lab}} \tag{5.18}$$

where m_p and m_T are mass of the proton (in amu) and target (aluminium)(in amu) respectively and E_r^{lab} is the laboratory resonance energy (in eV).

The resultant efficiencies from calibration sources and 10.762MeV resonance of the ^{27}Al(p,γ)^{28}Si reaction is shown in the Fig.5.3. The efficiency curve is fitted using the empirical formula [36]:

$$\ln(\eta_{ph}) = a + b\ln(E_\gamma) + c[\ln(E_\gamma]^2 \tag{5.19}$$

where E_γ is the γ-ray energy and a, b and c are free parameters. The efficiency curve is plotted in Fig. 5.3 and the fit parameters are shown in Tab. 5.2.

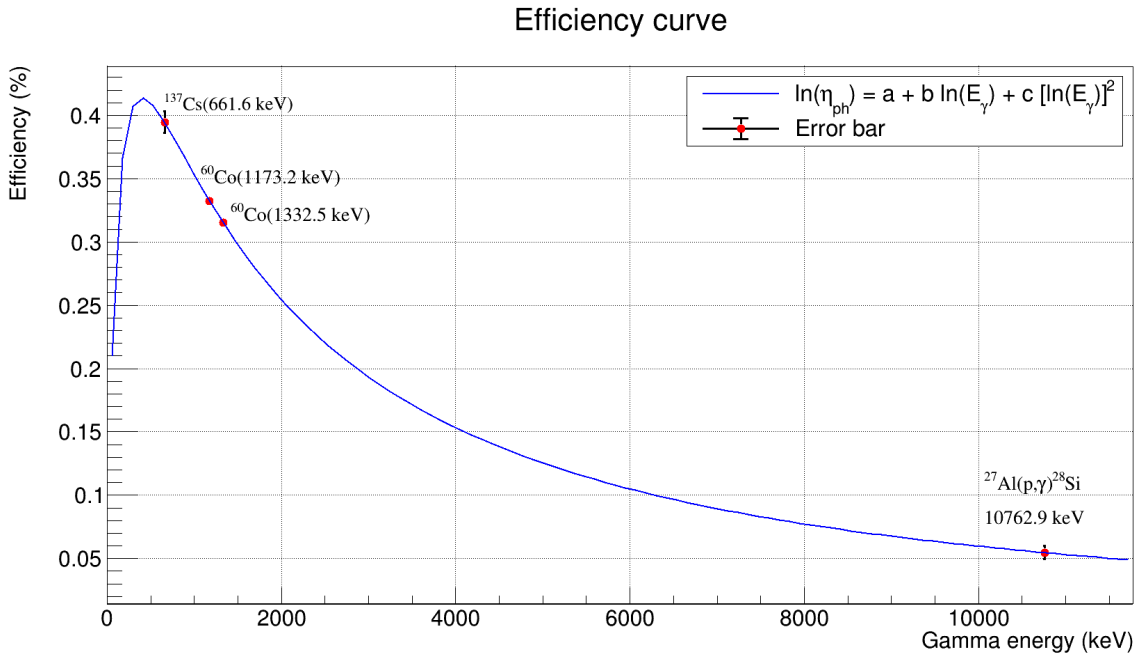

Figure 5.3: Efficiency curve obtained from calibration sources and $E_\gamma = 10.762$ MeV from 994.4 keV resonance of the ^{27}Al(p,γ)^{28}Si reaction.

a	b	c
-7.373(4)	2.1774(9)	-0.1821(1)

Table 5.2: Efficiency curve fit parameters

Using the obtained efficiency curve, we could calculate the efficiency of the E_γ from the ^{12}C (p,γ) ^{13}N reaction.

5.4 Target Characterization

In order to calculate the ^{12}C (p,γ) ^{13}N reaction S-factor, the target thickness, ΔE, and target composition, which eneter in the effective stopping power evaluation, are needed, see eq.5.3. Concerning the composition the nominal was assumed because evaporated natural carbon targets with 99% ^{12}C and 1% ^{13}C were used. In order to characterise and monitor the target thickness we performed a scan of ^{13}C (p,γ) ^{14}N (Q = 7550.56 keV) resonance at 1748 keV with resonance strength $\omega\gamma = (9.1 \pm 0.5)$ eV and width $\Gamma = (135 \pm 8)$eV. By increasing E_p by few keV run by run starting from 1746keV, we can match the resonance energy at different slices inside the target since the proton beam loses its energy. A γ-ray spectrum was obtained for each measurement of the resonance scan. The

region of interest (ROI) in the γ-ray spectra lies in E_γ = 8.0 - 9.4 MeV($E_\gamma \approx E_{cm} + Q$) which includes both the full-peak and the single and double-escape peaks of the direct transition to the ground state of the ^{14}N (see Fig.5.4).

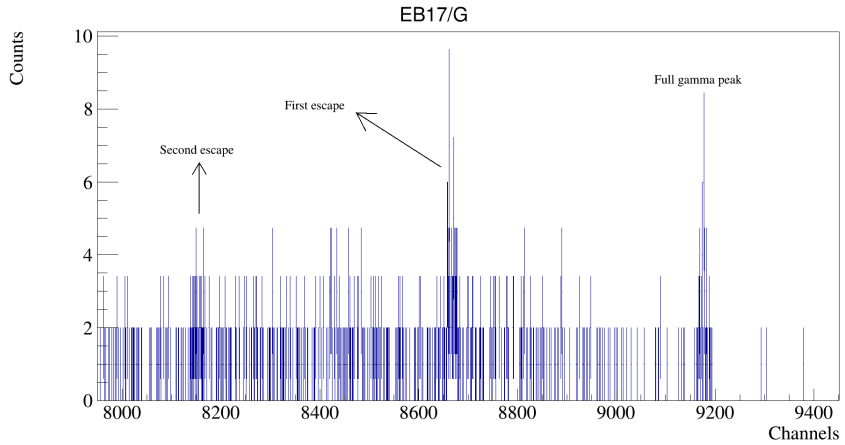

Figure 5.4: The region of interest for the analysis of the 1.748 Mev resonance of the ^{13}C$(p,\gamma)^{14}$N reaction exploited to characterize target thickness.

The target profile of T12C_L1 target obtained from the first resonance scan ^{13}C$(p,\gamma)^{14}$N is shown in Fig.5.5 . The experimental yield curve from the resonance scan, can be fit using the following empirical formula:

$$Y = Y_{max} \frac{1}{1 + e^{\frac{E_R - E_\gamma}{\delta_L}}} \frac{1}{1 + e^{\frac{E_\gamma - E_R - \Delta E}{\delta_R}}} \tag{5.20}$$

where ΔE is the target thickness, Y_{max} is the plateau height, δ_L and δ_R are the width of the rising and falling edge respectively. Using eq.5.20, the second scan of the T12C_L1 target and scan of T12C_L4 target profile are also fitted. The parameters of the fit for each scan are shown in Tab.5.3 which also includes the ΔE target thickness obtained from the fit and it is in good agreement with the nominal thickness values, and for target T12C_L1 no degradation is observed since the two scans give consistent thicknesses.

Target / Parameter	T12C_L1 first scan	T12C_L1 second scan	T12C_L4 scan
Y_{max} (arb. units)	0.041±0.0010	0.053±0.0017	0.054±0.0017
E_R (keV)	1747.10±0.0010	1746.9±0.0120	1747.10±0.0089
δ_L	0.089±0.0074	0.12±0.0011	0.076±0.0032
δ_R	1.05±0.0624	1.18±0.0635	1.35±0.1071
ΔE (keV)	4.540±0.136	4.48±0.1042	5.18±0.1150
Nominal thickness (keV)	≈ 4	≈ 4	≈ 5.5

Table 5.3: Fitted parameters for First scan, Second scan and L4 scan using eq.5.20.

These target profiles performed at E_p = 1746 - 1760 keV(Fig.5.5) cannot directly used in the calculation of the S-factor because these refers to $E_p \approx 1.74$ MeV this is higher than the ^{12}C (p,γ) ^{13}N reaction measurement performed at 350-700 keV proton energy range. So these target profiles were converted from energy units to physical units (atoms/cm^2)

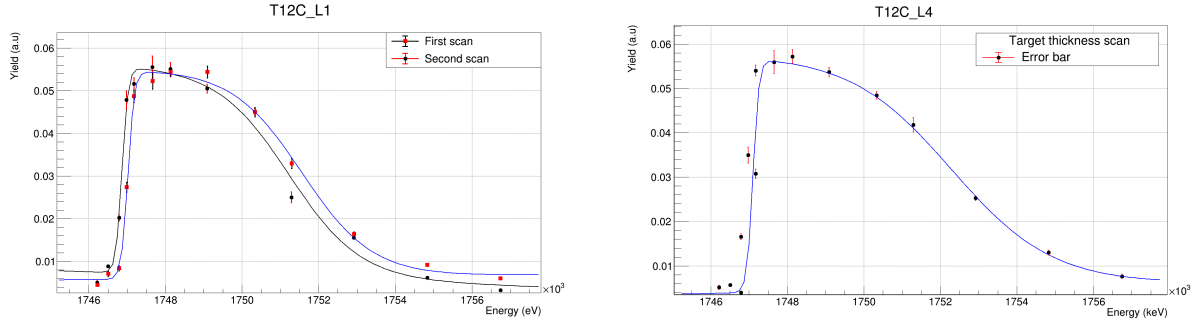

Figure 5.5: The first and second resonance scan with the target T12C_L1 are shown in left, the shift observed is due to the poor energy beam resolution. Right plot refers to the resonance scan with the target T12C_L4.

(see Fig.5.6), to have physical profile of the target that does not depend on energy. These conversion are done using the stopping power for proton beam of energy E_p = 1740 - 1760 keV in our carbon target. The stopping power which in this case match with effective stopping power, is calculated by eq.5.14. The converted target profile in proper units for both the targets are shown in Fig.5.6.

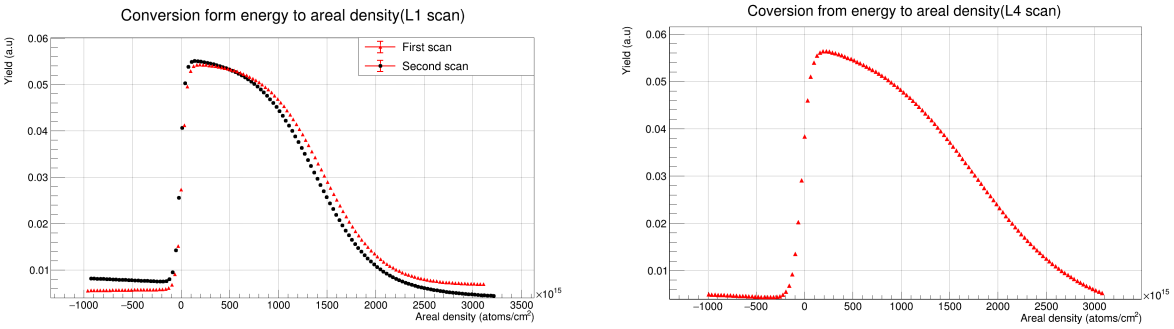

Figure 5.6: Each target scans(in Fig.5.5) are converted from ^{13}C (p,γ) ^{14}N reaction resonance energy units to physical units(atoms/cm^2) units. Left plots refer to the first and second resonance scan with the target T12C_L1 and right plot refers to the resonance scan with the target T12C_L4.

For S-factor calculation, the normalized target profile $P(E)$ has to be function of the proton beam, see eq.5.4. This calculation is done by converting the target profile with physical units (atoms/cm^2) to energy units by using effective stopping power. Each target profile is obtained in this way for each E_p investigated here. An example of target profile(normalised) for E_p = 400 keV is shown in Fig.5.7.

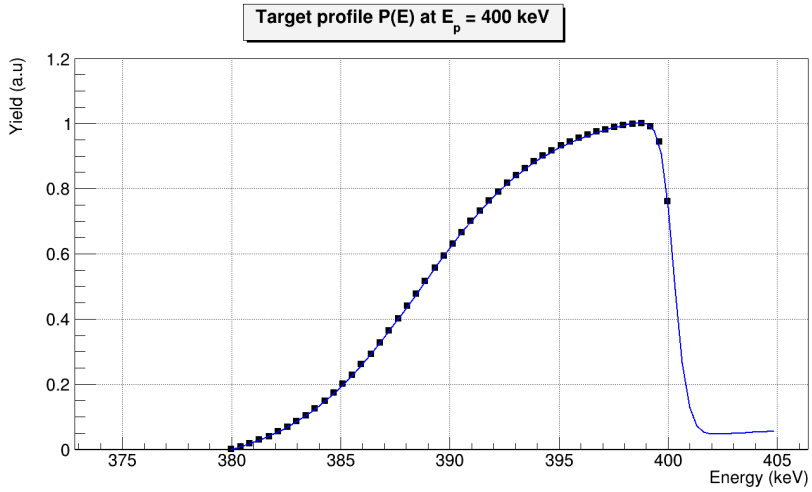

Figure 5.7: Normalised target profile is obtained by converting back from physical target profile to target profile in energy units at $E_p = 400$keV.

5.5 Yield Analysis for ^{12}C (p,γ) ^{13}N reaction

The energy calibration is the first step performed during the analysis. The energy calibration of the HPGe detectors used in the experiment was done using gamma rays coming from calibration sources and the proton capture reaction ^{27}Al(p,γ)^{28}Si. First, we will discuss the energy calibration performed using the calibration sources. The data of the calibration sources used is summarised in Table 5.4.

Source	Activity(kBq)	Photopeak (keV)	Branching ratio
^{60}Co	27.27(19)	1173.228(3) 1332.492(4)	0.9985(3) 0.999 826(6)
^{137}Cs	7.59(16)	661.659(3)	0.849(2)
^{22}Na	37.59(32)	511 1274.542(7)	1.807(2) 0.999(13)
^{88}Y	74.56(50)	898.042(11) 1836.070(8)	0.937(3) 0.99346(25)

Table 5.4: Data for the calibration sources used during the experiment.

In this experiment, the data of the calibration sources was acquired by the data acquisition channel DAQ2. The channel number for E_γ of calibration sources were obtained by doing a Gaussian fit to the γ-peak. In Fig.5.8, a gaussian fit performed for ^{137}Cs source is shown and the mean obtained from the fit is used as channel number for the calibration. To determine the relationship between γ-ray energy E_γ and spectrum channel number, a linear fit was performed :

$$E_\gamma = a + b * Channel \tag{5.21}$$

where a and b are the parameters that are needed to be determined.

The linear fit is shown in Fig.5.9 and its corresponding parameters are summarised in Tab.5.5 .

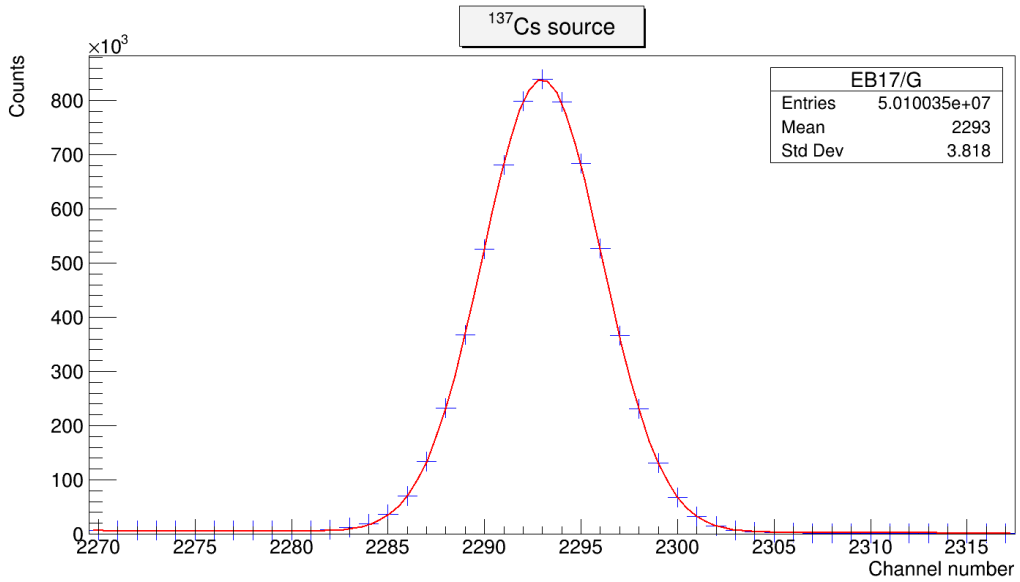

Figure 5.8: Gaussian fit performed for 661 keV γ-ray of ^{137}Cs source for calibration.

Acq. Channel	a	b	χ^2/dof
DAQ 2(sources)	0.56(3)	0.28854(8)	0.49

Table 5.5: Fit parameters for the HPGe detector calibration using the calibration sources mentioned in Tab.5.4.

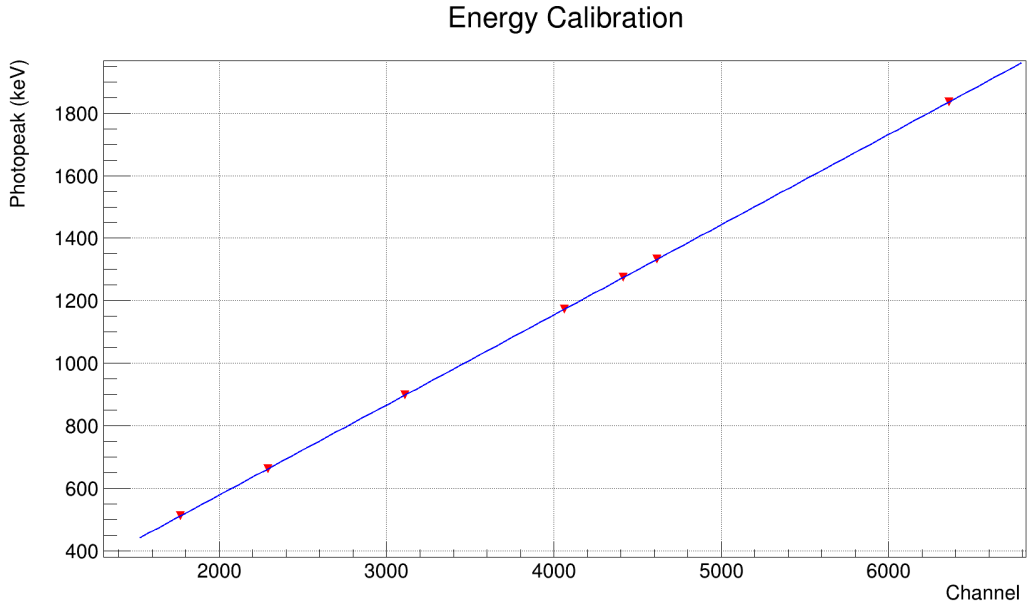

Figure 5.9: HPGe detector energy calibration fit for γ-ray sources mentioned in Table 5.4 using DAQ2.

As mentioned before, the energy calibration was also done using the gamma rays from ^{27}Al(p,γ)^{28}Si reaction and the data of this reaction is summarised in Table 5.6. In this case, both data acquisition channels DAQ1 and DAQ2 were used. Similar to the case of calibration sources, a linear fit (see 5.10) was also performed here between the gamma ray energy and channel number and the corresponding parameters are summarised in Table

5.7.

E_γ (keV)	E_i (keV)	E_f (keV)	Branching
1522.3	7798.8	6276.5	2.8±0.2
1778.9	1778.9	0	94.8±1.5
2838.9	4617.8	1778.9	5.5±0.4
4497.6	6276.5	1778.9	4.8±0.3
4608.4	r	7933.4	4.5±0.4
4743	r	7798.8	8.8±0.5
6019.9	7798.8	1778.9	6.0±0.5
6265.3	r	6276.5	2.1±0.2
10762.9	r	1778.9	76.6±1.5

Table 5.6: Data of γ-spectra from ^{27}Al(p,γ)^{28}Si reaction used in energy calibration. The r refers to resonance state in the ^{27}Al(p,γ)^{28}Si reaction at the Ep = 992 keV. [34].

Acq. Channel	a	b	χ^2/dof
DAQ 1(reaction)	6(56)	0.99(1)	762.26
DAQ 2(reaction)	0.73(4)	0.288544(8)	0.81

Table 5.7: Fit parameters for the HPGe detector calibration using the γ-ray from ^{27}Al(p,γ)^{28}Si reaction shown in Tab.5.6.

For ^{12}C (p,γ) ^{13}N reaction the Region of Interest lies between 2-3 MeV . The net counts in the γ-peak was obtained from the spectra by selecting the proper ROI. The expected position of the E_γ can be easily obtained by the following equation:

$$E_\gamma = Q + \frac{M}{m+M}E_p - \Delta E_{Rec} + \Delta E_{Dopp} \tag{5.22}$$

Where Q is the Q-value of the ^{12}C (p,γ) ^{13}N reaction (1943.5(3) keV), M and m are masses of ^{12}C and proton respectively, ΔE_{Rec} is the correction for the recoil effect of the ^{13}N compound nucleus and ΔE_{Dopp} is the correction for the Doppler effect. The recoil correction ΔE_{Rec} and Doppler correction ΔE_{Dopp} are defined as:

$$\Delta E_{Rec} = \frac{E_\gamma^2}{2M_{^{13}N}c^2} \;;\; \Delta E_{Dopp} = \frac{v}{c}E_\gamma cos\theta \tag{5.23}$$

where c is the speed of light, v is the compound nucleus velocity and θ is the angle between the beam direction and the γ-ray detector, which is 90^o for the detector(EB17) so the Doppler correction is zero.
In Fig.5.11, the ROI for the peak, whose shape also depend on the target thickness was selected by eye and a check on tail impact was performed, determining that the tail contributes only 1% to the net counts.

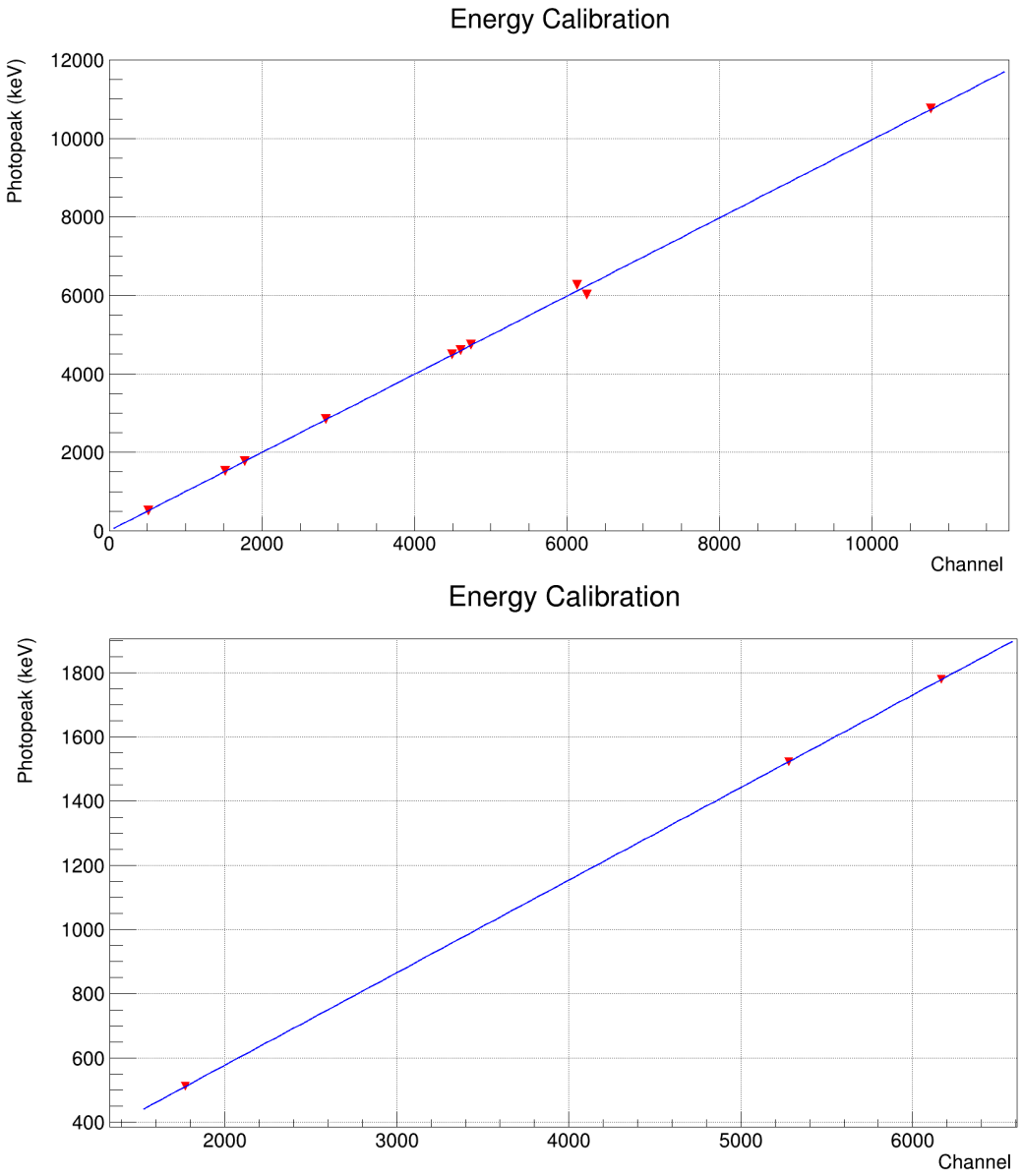

Figure 5.10: HPGe detector energy calibration fit for DAQ 1(top) and DAQ 2(bottom) with γ-rays from ^{27}Al(p,γ)^{28}Si reaction.

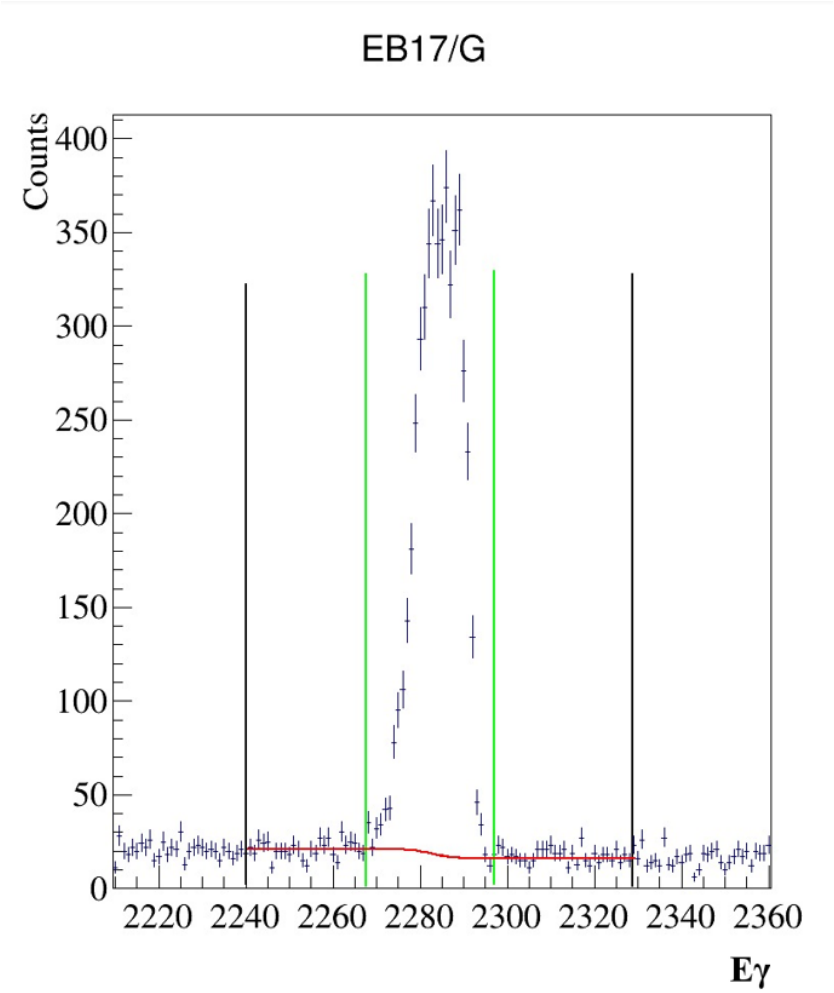

Figure 5.11: Direct capture γ-ray spectrum obtained at $E_p = 380$keV. ROI is between the green lines, and for the background suppression a sigmoidal error function is used which is presented in redline.

The net counts is calculated as the total number of the counts, N_T, subtracted by the number of counts in the background, N_B, which are determined as the area under the γ-peak define by a proper step like function fitting the background on the left and on the right of the ROI.

$$N_{counts} = N_T - N_B \tag{5.24}$$

$$\sigma^2_{counts} = \sigma^2_T + \sigma^2_B \tag{5.25}$$

where σ_{counts} is the calculated statistical error, and σ_T and σ_B are the error of the peak counts and background respectively.

For the calculation of the reaction yield, the number of the incoming protons,N_p, was calculated using the formula:

$$N_p = \frac{2 * Q_{run}}{e} \tag{5.26}$$

where the Q_{run} is the accumulated charge during each experimental run and e is the elementary charge.

The yields are calculated using the eq.5.1. The yield for both the targets (T12C_L1 and T12C_L4) for all the energy runs are shown in the Fig.5.12. The errors of the yield are only statistical.

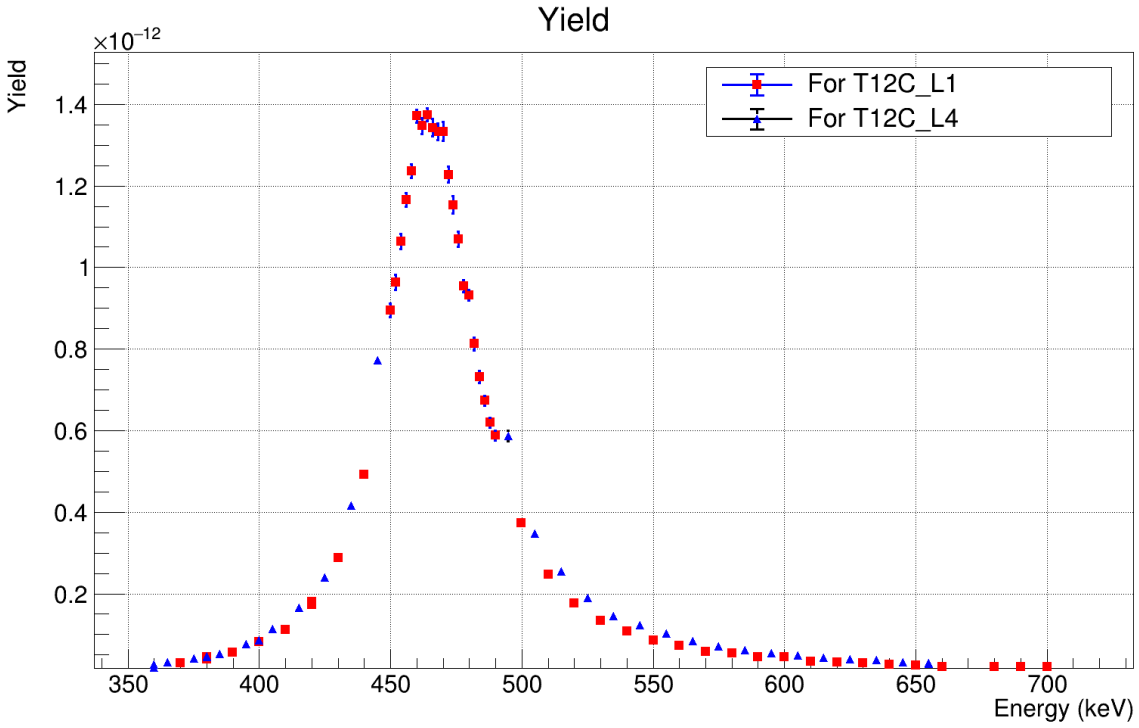

Figure 5.12: Yield for both the targets are plotted as a function of beam energy in lab frame. The red data points obtained for T12C_L1 target and blue data points for T12C_L4 target.

5.6 S-factor calculation

The S-factor was calculated using eq.5.5 for E_p = 350 - 700 keV. The effective stopping power, ϵ_{eff}, was calculated using the eq.5.14. The ΔE for the range of integration in S-factor calculation is obtained by taking the FWHM of normalized target profile, $P(E)$. The S-factor for both targets are shown in the Fig.5.13 and compared with literature data.

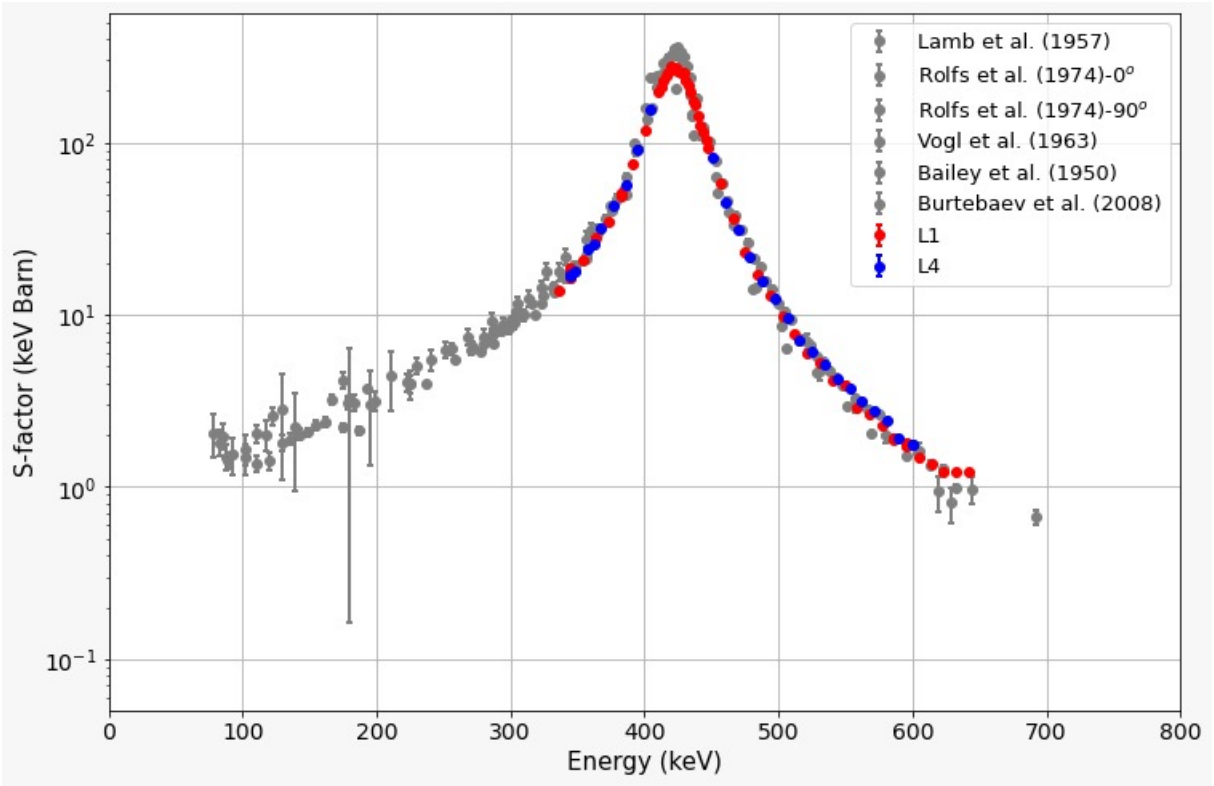

Figure 5.13: Comparison of preliminary S-factor calculation with data available in literature.

For the uncertainty of the S-factor, only statistical contribution, i.e. coming from the counting statistics and uncertainty in the calculation of the efficiency are included. The calculated values of the S-factor are in good agreement with literature. A comparison between the some values obtained in the present work with Vogl et al. [27] is performed and the consistency between two results are 10% while at the low energy the agreement is better but the Vogl et al. data is scattered more. Still, there is some discrepancy at resonance peak E_p = 457 keV. A future investigation is needed to study the discrepancy and resonance peak value.

Chapter 6
Conclusions and Outlook

The $^{12}C(p,\gamma)^{13}N$ reaction is the first channel of CNO cycle and it plays a crucial role in determining the abundances of the C isotopes in the stellar interiors. Especially, it has significant impact during the dredge-up episodes, i.e. mixing events caused by convective motion inside the stars which occurs at the end of the hydrogen burning, where the star enters its RGB phase, and at the end of the helium burning phase, when the star enters its AGB phase. To produce accurate theoretical models for the complex mixing mechanisms inside the stars, it is important to determine the reaction rate of the $^{12}C(p,\gamma)^{13}N$ and also reduce the uncertainties.

Present thesis reports on the experimental study of the S-factor of the $^{12}C(p,\gamma)^{13}N$ reaction in the wide energy range 350 - 700 keV with the help of five HPGe cluster detectors. The experiment was performed at the Felsenkeller underground facility in Dresden (Germany) using evaporated natural carbon targets (99% ^{12}C and 1% ^{13}C). The underground location guarantees an environmental background reduction enabling high sensitive measurements. The efficiency of the detector was obtained using the ^{137}Cs and ^{60}Co sources, and the $^{27}Al(p,\gamma)^{28}Si$ resonance at 994.4 keV. Scans of the 1747.6(9) keV resonance of the $^{13}C(p,\gamma)^{14}N$ reaction were performed to monitor and characterise the targets. Finally, the S-factor was obtained in the range 350 - 700 keV.

The present analysis is an attempt of calculation of the S-factor of $^{12}C(p,\gamma)^{13}N$ reaction. As discussed before the results obtained in the present work are in good agreement with the literature. Some of the future result to improve the present work are listed below:

- Some offline analysis of the target as RBS and ERDA can be performed in order to verify the composition of the target. In addition some online methods are available to cross-check the composition as determining the $^{12}C/^{13}C$ ratio from spectra or analyse the plateau of the $^{13}C(p,\gamma)^{14}N$ resonance scan.
- Some measurements were performed using thick graphite target. Analysis on thick graphite target is needed to check the consistency of the S-factor, and exclude any systematic effects due to target thickness.
- A cross-check between the Pulse Shape Analysis(PSA) [31] and target scan results for target projectile need to be performed.
- The summing correction for the detector efficiency needs to be added to improve the accuracy of the measurement. Additionally, a simulation code can be used for cross-checks and to assess the impact of any potential systematic effects.

- The data for the angular distribution needs to be analyzed to obtain a more complete understanding of the reaction mechanism and to verify the consistency of the obtained results.

Bibliography

[1] A. G. W. Cameron. Abundances of the elements in the solar system. *Space Science Reviews*, 15, Sept 1973.

[2] Michael Wiescher. Cosmic alchemy in the laboratory. *Physics*, 2:69, 8 2009.

[3] cococubed.

[4] C.E. Rolfs and W.S. Rodney. *Cauldrons in the Cosmos: Nuclear Astrophysics*. Theoretical Astrophysics. University of Chicago Press, 1988.

[5] Diego Vescovi. Nucleosynthesis of light and heavy elements across the galaxy. 2021.

[6] Daniel Bemmerer, Thomas E Cowan, Alexander Domula, Toralf Döring, Marcel Grieger, Sebastian Hammer, Thomas Hensel, Lisa Hübinger, Arnd R Junghans, Felix Ludwig, et al. The new felsenkeller 5 mv underground accelerator. In *Solar Neutrinos: Proceedings of the 5th International Solar Neutrino Conference*, pages 249–263. World Scientific, 2019.

[7] Miroslav Mocak, Simon Campbell, E. Mueller, and Konstantinos Kifonidis. The core helium flash revisited. iii. from population i to population iii stars. *http://dx.doi.org/10.1051/0004-6361/201014461*, 520, 09 2010.

[8] Peter Hoppe, Sachiko Amari, Ernst Zinner, Trevor Ireland, and Roy S Lewis. Carbon, nitrogen, magnesium, silicon, and titanium isotopic compositions of single interstellar silicon carbide grains from the murchison carbonaceous chondrite. *The Astrophysical Journal*, 430:870–890, 1994.

[9] D. Clayton. *Handbook of Isotopes in the Cosmos: Hydrogen to Gallium*. Cambridge Planetary Science. Cambridge University Press, 2003.

[10] E. Margaret Burbidge, G. R. Burbidge, William A. Fowler, and F. Hoyle. Synthesis of the elements in stars. *Rev. Mod. Phys.*, 29:547–650, Oct 1957.

[11] C. Iliadis. *Nuclear Physics of Stars*. Physics textbook. Wiley, 2015.

[12] Classifying Stars - The Hertzsprung -Russell Diagram.

[13] Falk Herwig. Evolution of asymptotic giant branch stars. *Annual Review of Astronomy and Astrophysics*, 43(1):435–479, 2005.

[14] Christopher Sneden. Cno abundances of stars undergoing first dredge up mixing. In *Symposium-International Astronomical Union*, volume 145, pages 235–245. Cambridge University Press, 1991.

[15] Oscar Straniero, Roberto Gallino, and Sergio Cristallo. s process in low-mass asymptotic giant branch stars. *Nuclear Physics A*, 777:311–339, 2006.

[16] Robert F Wing. *The Carbon Star Phenomenon*. Number 177. Springer Science & Business Media, 2000.

[17] Pavel A Denissenkov and Achim Weiss. Globular cluster archaeology: Hydrogen-burning nucleosynthesis and extra mixing in extinct stars. *The Astrophysical Journal*, 603(1):119, 2004.

[18] K Lodders, H Palme, and H-P Gail. Abundances of the elements in the solar system. *arXiv preprint arXiv:0901.1149*, 2009.

[19] Josep M TRIGO-RODRÍGUEZ, Domingo Aníbal GARCÍA-HERNÁNDEZ, Maria Lugaro, Amanda I Karakas, Mark van RAAI, Pedro García Lario, and Arturo Manchado. The role of massive agb stars in the early solar system composition. *Meteoritics & Planetary Science*, 44(5):627–639, 2009.

[20] N Langer, A Heger, S Wellstein, and F Herwig. Mixing and nucleosynthesis in rotating tp-agb stars. *arXiv preprint astro-ph/9904257*, 1999.

[21] Diego Vescovi, Sergio Cristallo, Maurizio Busso, and Nan Liu. Magnetic-buoyancy-induced mixing in agb stars: Presolar sic grains. *The Astrophysical Journal Letters*, 897(2):L25, 2020.

[22] Pavel A Denissenkov and Christopher A Tout. Partial mixing and formation of the 13c pocket by internal gravity waves in asymptotic giant branch stars. *Monthly Notices of the Royal Astronomical Society*, 340(3):722–732, 2003.

[23] HH Woodbury, AV Tollestrup, and RB Day. Low-energy gamma radiation from the bombardment of carbon by protons. *Physical Review*, 93(6):1311, 1954.

[24] Carl L Bailey and William R Stratton. Cross section of the c 12 (p, γ) n 13 reaction at low energies. *Physical Review*, 77(2):194, 1950.

[25] Robert Noel Hall and William Alfred Fowler. The cross section for the radiative capture of protons by c 12 near 100 kev. *Physical Review*, 77(2):197, 1950.

[26] WAS Lamb and Ross E Hester. Radiative capture of protons in carbon from 80 to 126 kev. *Physical Review*, 107(2):550, 1957.

[27] Joseph L Vogl. *Radiative capture of protons by C12 and C13 below 700 keV*. PhD thesis, California Institute of Technology, 1963.

[28] C Rolfs and RE Azuma. Interference effects in 12c (p, γ) 13n and direct capture to unbound states. *Nuclear Physics A*, 227(2):291–308, 1974.

[29] N Burtebaev, SB Igamov, RJ Peterson, R Yarmukhamedov, and DM Zazulin. New measurements of the astrophysical s factor for 12 c (p, γ) 13 n reaction at low energies and the asymptotic normalization coefficient (nuclear vertex constant) for the p+ 12 c$\rightarrow$ 13 n reaction. *Physical Review C*, 78(3):035802, 2008.

[30] Tamás Szücs, Daniel Bemmerer, Detlev Degering, Alexander Domula, Marcel Grieger, Felix Ludwig, Konrad Schmidt, Julia Steckling, Steffen Turkat, and Kai Zuber. Background in γ-ray detectors and carbon beam tests in the felsenkeller shallow-underground accelerator laboratory. *The European Physical Journal A*, 55(10):1–12, 2019.

[31] Giovanni Francesco Ciani et al. Cross section of the 13c (a, n) 16o reaction at low energies. 2019.

[32] Glenn F Knoll and F Glein. Radiation detection and measurement, wiley. *New York*, 1989.

[33] James Ziegler - SRIM TRIM.

[34] A Antilla, Juhani Keinonen, M Hautala, and I Forsblom. Use of the 27al (p, γ) 28si, ep= 992 kev resonance as a gamma-ray intensity standard. *Nuclear Instruments and Methods*, 147(3):501–505, 1977.

[35] Christian Iliadis, Richard Longland, AE Champagne, and Alain Coc. Charged-particle thermonuclear reaction rates: Iii. nuclear physics input. *Nuclear Physics A*, 841(1-4):251–322, 2010.

[36] Glenn F Knoll. *Radiation detection and measurement*. John Wiley & Sons, 2010.